IEET

International Electrical Engineering Transactions

Vol. 3 No. 2 (5)
July - December, 2017
ISSN 2465-4256

An online publication of the EEAAT
Electrical Engineering Academic Association (Thailand)
www.journal.eeaat.or.th

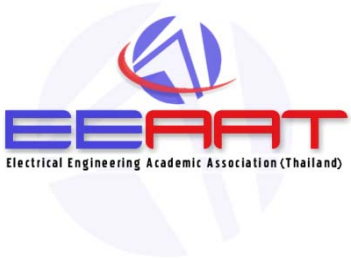

IEET – International Electrical Engineering Transactions

This journal is an online publication of the EEAAT, Electrical Engineering Academic Association (Thailand). IEET is published twice a year, ie., the first issue is for January – June and the second issue is for July – December.

EEAAT Journal Committee

IEET Editors

IEET (International Electrical Engineering Transactions) is published twice a year. Original contributions covering work in all aspects of electrical science, technology, engineering, and applications will be peer-reviewed by experts before publication. Topics of interest include the following: electrical power, electronics, telecommunication, control and system, sensor and measurement, optical technology, computer, information and communication technology (ICT), signal processing, social network tools and applications (apps), engineering education and other related fields.

For online submission of all manuscripts, correspondences, and letters, please visit
www.journal.eeaat.or.th

IEET Editorial Office

EEAAT - Electrical Engineering Academic Association (Thailand)
Room 409, F-Building,140 Cheum-Sampan Rd.
Nong Chok, Bangkok, Thailand 10530
Tel: +662-988-3655 ext 2216 Fax: +662-988-4026

IEET - International Electrical Engineering Transactions
Volume 3
Number 2 (5)
July – December 2017

PAPERS

Design of Printed Ultra-wideband Antenna with High Performance Notching Bands

Pichet Moeikham
Department of Electrical Engineering, Faculty of Engineering, Rajamangala University of Technology Lanna
Chiang-Rai, Thailand

Nonchanutt Chudpooti and Prayoot Akkaraekthalin
Department of Electrical and Computer Engineering, Faculty of Engineering,
King Mongkut's University of Technology North Bangkok
Bangkok, Thailandline

***Abstract*—This paper proposes the design of printed ultra-wideband monopole antenna with high performance band notching. The inverted L-shaped and modified U-shaped narrow slits embedded on the monopole patch were utilized to reject the undesired frequency bands at 3.5 GHz and 5.5 GHz, which their lengths corresponded to quarter and half wavelengths at those frequencies, respectively. The CPW feed comprised of both gradual central line and ground plane was used. The proposed antenna could be operated at the frequency band of 2.8-11 GHz covering the current UWB system except the frequency bands of 3.3-3.9 GHz and 5.1-5.7 GHz. The proposed antenna was completely implemented and measured showing the potential to minimize EMIs in the WLAN/WiMAX bands.**

Keywords— Band notching; printed UWB antenna; inverted L-shaped; modified U-shaped

I. INTRODUCTION

Since the printed antennas had been emerged, there are rapid growths of modern mobile applications. Because of low profile and compact size of the printed antennas, they have been popularly used for small handheld mobile devices. Additionally, with the advantages of various shape designing and ease for matching with RF and microwave circuits, the printed antennas can be capably operated with extremely large bandwidth or ultra-wideband (UWB) [1-6]. The UWB systems usually employ impulse signals, resulting in high data rate.

Therefore, they are prominently employed for short-range communications including body area and wireless sensor networks. The standard of ultra-wideband communications occupying the frequency range from 3.1 to 10.6 GHz allocated by Federal Communications Commission (FCC) has been used for indoor short-range communications [7]. As known, wireless local area network (WLAN) and worldwide interoperability for microwave access (WiMAX) are operated at frequency bands of 2.4-2.48/5.15-5.35/5.725-5.825 GHz and 3.3-3.6/5.15-5.825 GHz, respectively. Cleary, the UWB spectrum covers very wide bandwidth and the existing bands of WLAN/WiMAX systems are overlapping within the UWB frequency band. This may lead to electromagnetic interference (EMI) and becomes a major problem for wireless communication systems. In order to reduce the EMI, several UWB antennas with band-notched characteristics have been proposed. Many techniques have been employed to design the UWB antennas with band notching structures. Recently, the monopole UWB antennas with multiple split-ring resonators were proposed in [8]-[9]. A printed planar monopole UWB antenna with band notching characteristic was designed by using annular slot for 5.5 GHz band notching [10]. A rectangular patch UWB antenna with a small rectangle patch on another side of substrate for band notched characteristic was also proposed in [11]. A trapezoidal patch dipole antenna was designed with embedded T-shaped slot into the patches for frequency band notching [12]. A compact Bluetooth/UWB antenna was also designed using rectangular resonant spiral structures for quadruple frequency band rejection [13]. Although, aforementioned antennas were designed with compact sizes [8-14], those antennas were implemented using both sides of substrates leading to complicated structures when interfacing with other RF and microwave circuits and SMD devices. Moreover, the antennas in [8-13] were not designed for the frequency notched band of 3.5 GHz, the major interference band.

In this paper, the printed UWB antenna with rejection bands of 3.5 and 5.5 GHz bands is proposed. The proposed antenna is designed on only one side of the FR4 substrate occupying conductor dimensions of 34×19.22 mm2. The UWB antenna in [15] is used to be a baseline antenna providing impedance bandwidth covering UWB frequency. To reduce the effect of EMIs at the operating frequency bands of 3.5 and 5.5 GHz existing for the WLAN/WiMAX systems, these frequency bands must be notched. Two narrow slits are used to achieve the notched bands. The design procedures of the proposed antenna and parameter study are given. Also, the simulated and measured results are compared.

II. ANTENA DESIGN

A. Design Procedure

The proposed antenna was optimized by using the CST microwave studio software. Firstly, the UWB antenna in [15] was employed as baseline antenna. The gradual curvature structures of feeding section and ground plane were carefully designed, resulting in extremely large bandwidth. This antenna

was then developed on the conventional FR4 substrate with thickness of 0.8 mm, dielectric constant of 4.4 and loss tangent of 0.019. As shown in Fig.1 (a), the CPW was employed as the feeding system. The optimized gradual tapered central feed line and CPW ground planes were used for good impedance matching. The optimal dimensions of 34×19.22 sq.mm were achieved. The antenna covers for UWB frequency operation and also the size is very compact. The simulated |S11| results of all antenna designs are shown in Fig. 2. It is seen that the baseline antenna provides the operating frequency range of 2.7 GHz to exceed 12 GHz with the |S11| ≤ -10 dB covering UWB applications. Secondly, to eliminate the EMI at the frequency band of 3.5 GHz, the baseline antenna was also modified. As shown in Fig.1 (b), an invert L-shaped narrow slit was embedded into the antenna patch. The frequency rejection range of 3.3-3.7 GHz was obtained, as the |S11| values shown in Fig. 2. The invert L-shaped narrow slit length is approximate a quarter wavelength (λg/4) at the frequency of 3.5 GHz corresponding to equation (1). Although, the antenna capably reduces the EMI at the WiMAX frequency band of 3.5 GHz, the existing frequency of WLAN/WiMAX from 5.15-5.85 GHz still interferes the UWB band. This frequency band must be rejected. Finally, to reduce the EMI at the frequency of 5.5 GHz band, a modified U-shaped narrow slit was carefully introduced and embedded nearly radiating part, as shown in Fig.1 (c). It is found that after embedding the modified U-shaped narrow slit, the frequency rejection at 5.5 GHz band is achieved. The overall length of the modified U-shaped narrow slit (2×U2+U1) is about a half wavelength (λg/2) at the frequency of 5.5 GHz corresponding to equation (1), where λg and εr are the wavelength and the dielectric constant of substrate, respectively.

$$\lambda_g \approx \frac{3\times10^8}{fontch\sqrt{\left(\left(\varepsilon_r+1\right)/2\right)}} \qquad (1)$$

It is clearly seen in Fig.2 that the antenna in Fig.1 (c) with the embedded inverted L-shaped and the modified U-shaped narrow slits has ability to reduce the EMIs at frequency bands of 3.3-3.7 GHz and 5.2-5.8 GHz, respectively. Therefore, the proposed antenna was then constructed. The antenna schematic is now shown in Fig.3. All optimal dimensions are shown as follows: w1 = 0.4, L1 = 11.5, L2 = 2, L3 = 1.25, U1 = 3, U2 = 8.25, and U3 = 14.5. All dimension units are in millimeter.

It was obviously seen that when the narrow slits were embedded into the patch, there were several effects on the antenna characteristics. On the other words, the length and position of these narrow slits were the major effects on the band notching of the antenna. To see these effects, the major parameters were then carefully studied by varying the values of parameter.

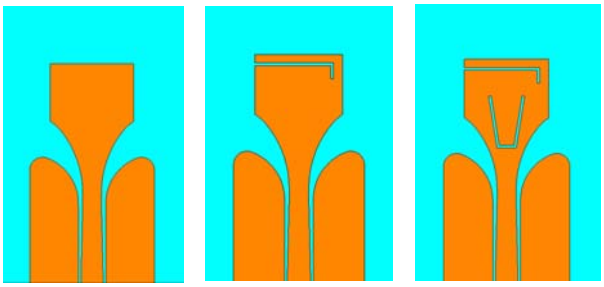

Fig.1 *Steps of designing the proposed antenna.*

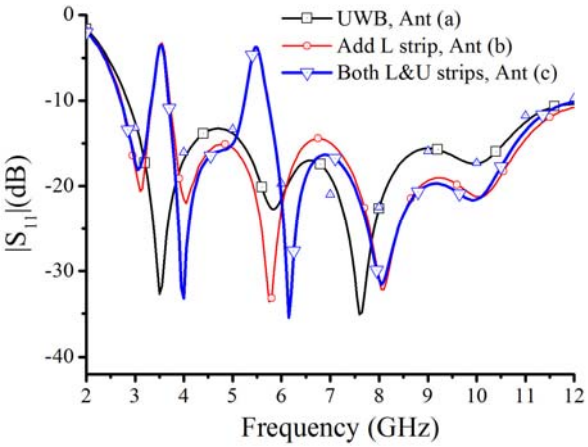

Fig.2 *Simulated |S11| results of the antennas.*

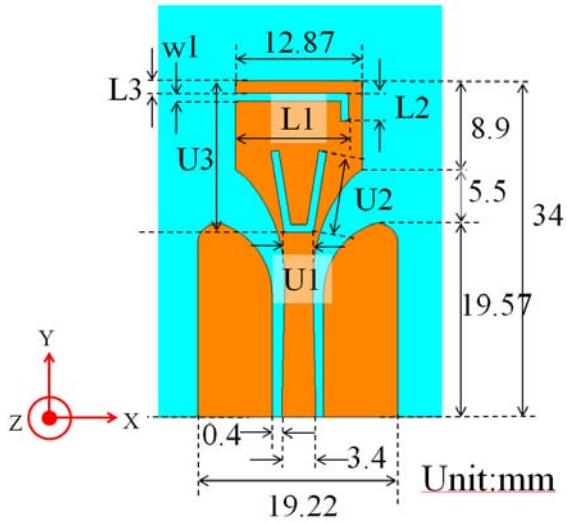

Fig.3 *Layout of the proposed antenna.*

B. Effects of Inverted L-Shaped Narrow Slit

When the inverted L-shaped narrow slit was embedded into the patch of the proposed antenna, the frequency notched band at 3.5 GHz was obtained. It is found that the resonance of rejected frequency depends on the length of narrow slit, corresponding to equation (1). Fig.4 (a) depicts the simulated |S11| results when the length of narrow slit (L1) was varied whereas the other parameters were fixed. The rejected frequency at the band of 3.5 GHz shifted to lower side frequency when the L1 parameter was increased and vice versa. The optimal L1 of 11.5 mm which overall length (L1+L2) is 13.1 mm, results in the rejected frequency band of 3.3-3.7 GHz. The length of inverted L-shaped narrow slit is about a quarter wavelength at 3.5 GHz (13.55 mm).

As early mentioned, the length of narrow slit capably controls the resonance of rejected frequency. From simulated results, it is found that the position of narrow slit (L3) controls the notched bandwidth. The position of narrow slit is defined as distance between the narrow slit and the top edge of patch which is denoted by the L3, as shown in Fig.3. Fig.4 (b) depicts the simulated |S11| results when L3 was varied while the other parameters were fixed. It is clearly seen that when L3 was increased, the notched bandwidth extended. The effect is caused from the increment of electromagnetic coupling between radiating part and narrow slit when L3 was increased and vice versa. Obviously, both sides of the patch are main current paths for radiating the electromagnetic waves. When the path is obstructed by the narrow slit, the current path changed. The electromagnetic energy is absorbed by the narrow slit, and then the frequency rejection is achieved. It is found that the optimal L3 of 1.25 mm provides the notched bandwidth of 0.4 GHz or rejected frequency band of 3.3-3.7 GHz, which is appropriate for applications.

C. Effects of Modified U-Shaped Narrow Slit

In order to reject the frequency band at about 5.5 GHz, the modified U-shaped narrow slit was embedded into the patch, as shown in Fig.1 (c). By adjusting the length of modified U-shaped narrow slit or U2, the resonance of rejected frequency altered. Fig.5 (a) shows the |S11| simulated results when the length of U2 was varied. It is clearly seen that when the value of U2 parameter was increased, the resonant of rejected frequency shifted to lower side frequency and vice versa. The appropriate U2 parameter of 8.25 mm, resulting in average

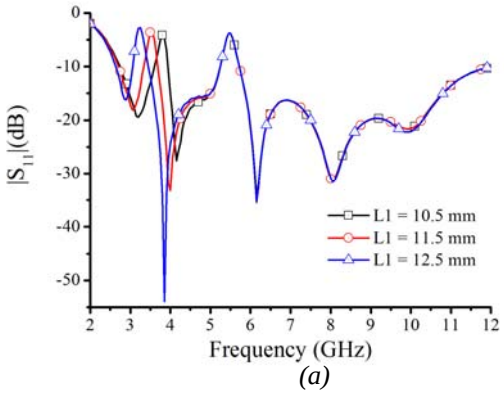

(a)

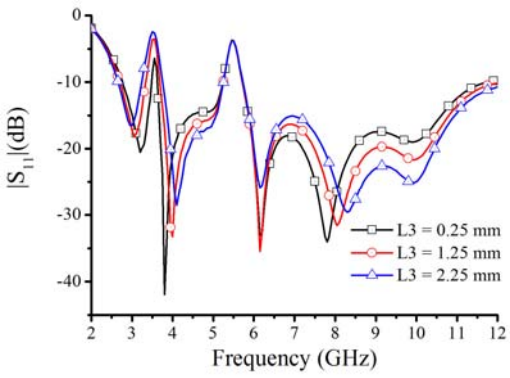

(b)

Fig. 4 *Simulated results of |S11| when varying parameters of (a) L1 and (b) L3.*

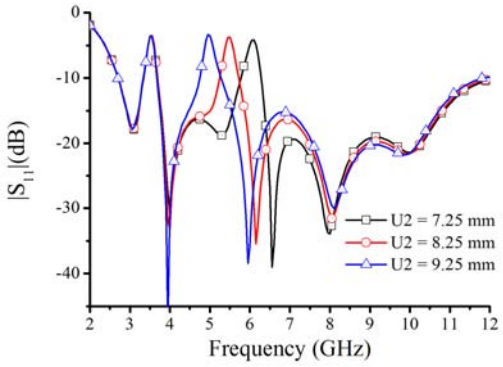

(a)

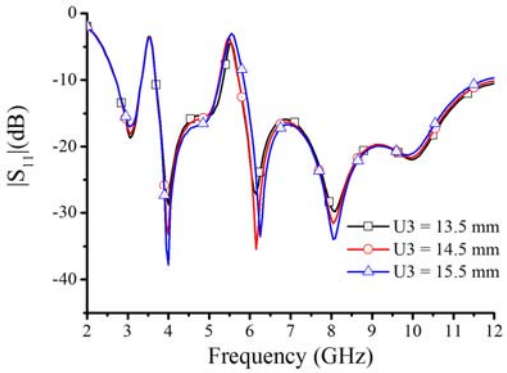

(b)

Fig.5 *Simulated results of |S11| when varying parameters of (a) U2 and (b) U3.*

overall length (2×U2+U1) of 18.7 mm, provides the rejected frequency band at 5.5 GHz. Additionally, this length is approximately a half wavelength at the frequency of 5.5 GHz or 17.3 mm, corresponding to equation (1).

It is clearly seen that the length of narrow slit, U2, can control the center frequency of the second rejected frequency at 5.5 GHz band. The notched bandwidth can be controlled by the position of modified U- shaped narrow slit. This position is determined by the distance between the narrow slit and the top

edge of patch, which is denoted by U3. On the other words, the position of narrow slit changed by varying U3 parameter. The simulated result of |S11| when varying the position U3 are shown in Fig.5 (b). The results confirms that when the narrow slit is placed far away from the top edge of the patch, the notched bandwidth slightly extends and vice versa. This is because the electromagnetic coupling between radiating part and the narrow slit is increased or more amount of electromagnetic energy is stored by the narrow slit when the narrow slit is moved close to the radiating part (U3 is increased) and vice versa. Besides, the center of rejected frequency slightly shifts to higher side frequency when U3 parameter is increased and vice versa. The optimal U3 of 14.5 mm provides the proper notch with bandwidth of about 0.5 GHz or the rejected frequency range is 5.2-5.7 GHz.

D. Surface Current Distributions

As mentioned, to understand about the notched frequency mechanism, surface current distributions on the antenna structure can be determined and used for explanation. Figs.6 (a) and (b) display the surface current distributions at the operating frequencies of 4.5 GHz and 8.5 GHz, respectively. It can be seen that the strong surface current density distributes along the edge of conductor including the patch and the ground plane, whereas the moderate current density is diminished at adjacent area. At middle of the patch, there is almost no current density. These operating mechanisms produce major current paths around the patch which is the resonance part; therefore, electromagnetic wave was capably radiated from the antenna.

The current distributions on the designed antenna at the notched frequencies of 3.5 GHz and 5.5 GHz are shown in Figs.7 (a) and (b), respectively. At the frequency of 3.5 GHz, it is found that the strong surface current density is mostly concentrated at the L-shaped narrow slit while there is a little surface current on the other areas. At the frequency of 5.5 GHz, the surface current distribution shows as same property as the notched frequency of 3.5 GHz. The electromagnetic energy is absorbed when current distribution is highly concentrated at both narrow slits. As a result, there is no radiation of electromagnetic wave from the antenna. On the other words,

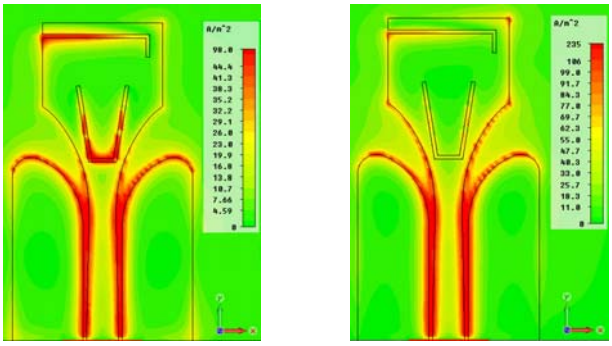

(a) (b)

Fig.6 *Simulated surface current distributions at frequencies of (a) 4.5 GHz and (b) 8.5 GHz.*

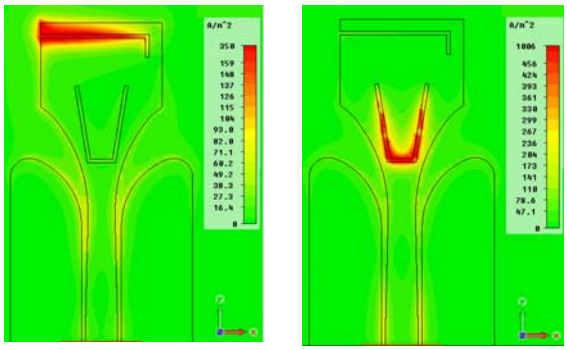

(a) (b)

Fig.7 *Simulated surface current distributions at the notched frequencies of (a) 3.5 GHz and (b) 5.5 GHz.*

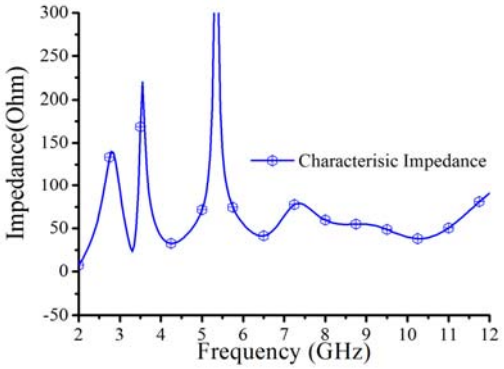

Fig.8 *Simulated result of the characteristic impedance.*

when almost current density is stored by both narrow slits, the characteristic impedances at notched frequencies of 3.5 GHz and 5.5 GHz are acutely changed, leading to some mismatches at the antenna input. Fig.8 displays the simulated characteristic impedance of the designed antenna. It is clearly seen that the input impedance is drastically changed at both notched frequencies of 3.5 and 5.5 GHz while there are nearly constant at other operating frequencies. Because of this, the proposed antenna cannot radiate the electromagnetic waves at those notched frequencies.

III. RESULT AND DISCUSSION

All optimal parameters were employed for fabricating the prototype antenna by using chemical wet etching on the FR4 substrate with thickness of 0.8 mm, dielectric constant of 4.4 and loss tangent of 0.019. Fig.9 shows the photograph of prototype antenna. The SMA connector was used to feed the antenna for the measurement purpose. The measurement was then accomplished in anechoic chamber room. All measured results of |S11|, |S21|, radiation patterns, group delay time and antenna gain will be described and discussed in details in the following subsections.

A. *Simulated and measured |S11| results*

A comparison between the simulated and measured results of |S11| is now shown in Fig.10. From the measured result, it is found that the lower edge frequency is slightly shifted to higher frequency about 0.2 GHz while the higher edge frequency is gradually decreased to 11 GHz. The first and second rejected frequencies are occurred at 3.5 GHz and 5.5 GHz, respectively, which coincide with the simulated results. Although, there are some discrepancies causing from discontinuity from the SMA connector to CPW transmission line and fabrication tolerance, the measured result of |S11| still agrees well with the simulation. Two rejected frequency bands were obtained from the prototype antenna with the ranges of 3.3-3.9 GHz and 5.1-5.7 GHz. This result confirms that the proposed antenna *has a strong potential to reduce the EMIs at these bands.*

Fig.9 *Photograph of the prototype antenna.*

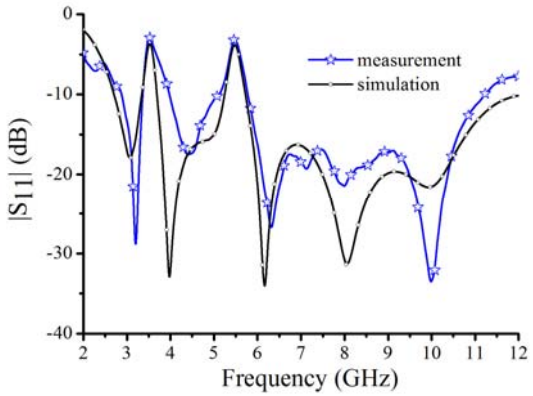

Fig.10 *A comparison of the simulated and measured results of |S11|.*

B. *Radiation Patterns*

The measured radiation patterns in xz and yz planes are shown in Fig.11 and Fig.12, respectively. The results confirms that the proposed antenna provides co-polarization radiation pattern nearly omnidirectional in xz plane at all frequency bands, However, as shown in Fig.12, a likely bi-directional adiation pattern is given in yz plane by the proposed antenna at the same frequencies. Nevertheless, some distortions are found at higher frequencies because of the higher mode operation of the antenna. Additionally, the high cross polarization is appeared because of the curvature current path of the antenna structure.

C. *Transfer function, group delay time and gain*

Fig.13 depicts the measured transfer function or |S21| and group delay time of the proposed prototype antenna. By placing face to face of two identical antennas with a distance of about 35 mm, the time domain measurement was accomplished. It is seen that the |S21| sharply drops to -54 dB and -56 dB at resonances of rejected frequencies of 3.5 GHz and 5.5 GHz, respectively. The average of group delay time is about 1.7 ns at the operating band, showing rather constant. The linear phase response is also obtained and sufficient to use for impulse transmission. At two notched frequencies, the proposed antenna provides the group delay time of 2.67 ns, indicating discontinuity phase at these bands.

The measured broadside gain of the proposed antenna is also shown in Fig.14. It is found that the operating bands are appeared with frequency ranges of 3.1-3.3 GHz, 3.8-5.1 GHz and 5.9-10.6 GHz, respectively. The maximum broadside gains are -1.9 dB, 0.64 dB and 2.35 dB, respectively. A little fluctuation is found at the higher frequency band, which the electromagnetic disturbance generated by the narrow slits may cause of this effect.

IV. CONCLUSIONS

The compact printed UWB antenna with notched bands at 3.5 and 5.5 GHz was proposed. The tapered central feed line of CPW was employed for impedance matching enhancement. By embedding the inverted L-shaped narrow slit on the patch, the frequency band of the WiMAX system at 3.5 GHz was rejected. Also, by embedding the modified U-shaped narrow slit nearby curvature part on the patch, the frequency band of the WLAN/WiMAX systems at of 5.5 GHz was rejected. The operating frequency band of 2.8-11 GHz covering UWB system was obtained by the proposed antenna except the frequency bands of 3.3-3.9 GHz and 5.1-5.7 GHz. The resonance frequency of rejected band could be controlled by the length of narrow slit. Also, the notched bandwidth was controlled by the position of narrow slit on the patch. Additionally, the proposed antenna provided the group delay time nearly constant of less than 2 ns suitable for using with impulse transmission.

V. ACKNOWLEDGMENT

This work has been supported by Thailand Research Fund through the TRF Senior Research Scholar Program with the Grant No. RTA6080008.

REFERENCES

[1] H. R. Khaleel, "Design and fabrication of compact inkjet printed antennas for integration within flexible and wearable electronics," IEEE Trans. Compon. Packag. Manuf. Technol., vol. 4, no. 10, pp. 1722-1728, Oct. 2014.

[2] Y. Wang, F. Zhang, G. Fang, Y. Ji, S. Ye and X. Zhang, "A novel ultrawideband exponentially tapered slot antenna of combined electric-magnetic type," IEEE Antennas Wireless Propag. Lett., vol.15, pp.1226-1229, 2016

[3] J. Wu, Z. Zhao, Z. Nie and Q. H. Liu, "A printed UWB Vivaldi antenna using stepped connection structure between slotline and tapered patches," IEEE Antennas and Wireless Propag. Lett., vol.13, pp.698-701, 2014.

[4] M. C. Tang, T. Shi and R. W. Ziolkowski, "Planar ultra-wideband antennas with improved realized gain performance," IEEE Trans. Antennas Propag., vol.64, no.1, pp.61-69, Jan. 2016.

[5] G. Bozdag and A. Kustepeli, "Subsectional tapered fed printed LPDA antenna with a feeding point patch," IEEE, Antennas and Wireless Propag. Lett., vol.15, pp.437- 440, 2016.

[6] M. S. Ellis, Z. Zhao, J. Wu, Z. Nie and Q. H. Liu, "Small planar monopole ultra-wideband antenna with reduced ground plane effect," IET Micro. Antennas Propag., vol.9, no.10, pp.1028-1034, Jul. 2015.

[7] Federal Communications Commission, Washington, DC, USA, "Federal Communication Commission revision of Part 15 of Commission's rules regarding ultra-wideband transmission systems," First Report and Order FCC, 02.V48, 2002.

[8] Siddiqui, J.Y.; Saha, C.; Antar, Y.M.M., "Compact SRR loaded UWB circular monopole antenna with frequency notch characteristics," IEEE Trans. Antennas Propag., vol.62, no.8, pp.4015-4020, Aug. 2014.

[9] Siddiqui, J.Y.; Saha, C.; Antar, Y.M.M., "Compact dual-SRR-loaded UWB monopole antenna with dual frequency and wideband notch characteristics," IEEE Antennas and Wireless Propag. Lett., vol.14, pp.100-103, 2015.

[10] R. Azim and M. T. Islam, "Compact planar UWB antenna with band notch characteristics for WLAN," Progress Electromag. Research, vol.133, pp.391-406, 2013.

[11] Thomas, K.G.; Sreenivasan, M., "A simple ultrawideband planar rectangular printed antenna with band dispensation," IEEE Trans. Antennas Propag., vol.58, no.1, pp.27- 34, Jan. 2010.

[12] Y.-S. Hu, M. Li, G.-P. Gao, J.-S. Zhang, and M.-K. Yang, "A double-printed trapezoidal patch dipole antenna for UWB applications with band-notched characteristic," Progress Electromag. Research, vol.103, pp.259-269, 2010.

[13] Reddy, G.S.; Kamma, A.; Mishra, S.K.; Mukherjee, J., "Compact Bluetooth/UWB Dual-Band Planar Antenna With Quadruple Band-Notch Characteristics," IEEE Antennas and Wireless Propag. Lett., vol.13, pp.872-875, 2014.

[14] S. M. Abbas, Y. Ranga, A. K. Verma and K. P. Esselle, "A simple ultra wideband printed monopole antenna with high band rejection and wide radiation patterns," IEEE Trans. Antennas Propag., vol.62, no.9, pp.4816-4820, Sept. 2014.

[15] Moeikham, P.; Akkaraekthalin, P., "A compact ultrawideband monopole antenna with tapered CPW Feed and slot stubs," in Electrical Engineering/ Electronics, Computer, Telecommunications and Information Technology (ECTI-CON), 2011 8th Internat. Conf., pp.180-183, 17-19 May 2011.

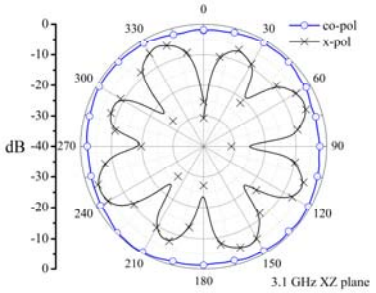

(a)

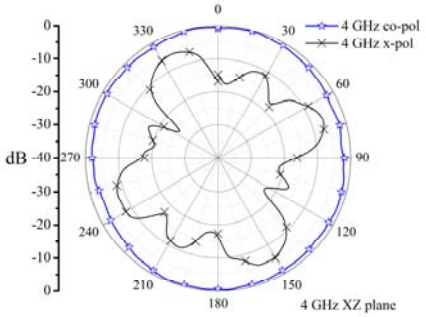

(b)

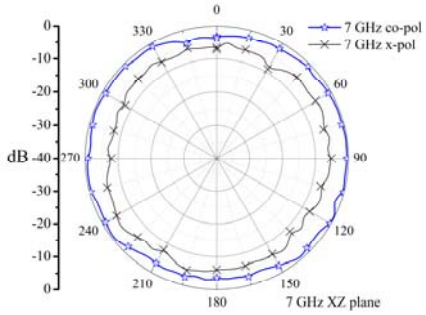

(c)

Fig.11 *Measured radiation pattern results in xz plane at frequencies of (a) 3.1 GHz, (b) 4 GHz and (c) 7 GHz.*

Review Study of Maximum Power Point Tracking Algorithms for PV system

Anuchit Aurairat
Department of Electrical Engineering, Faculty of Engineering Rajamangala University of Technology Thanyaburi
Thanyaburi , Thailand
e-mail: anuchit_a@mail.rmutt.ac.th

Boonyang Plangklang
Department of Electrical Engineering, Faculty of Engineering Rajamangala University of Technology Thanyaburi
Thanyaburi , Thailand
e-mail: boonyang.p@en.rmutt.ac.th

***Abstract*— The energy produced by the solar cells is more widespread in the production of renewable energy, which is clean, reliable and secure. The most important component is the technology of inverter that converts the direct current from photovoltaic array into alternating current, which has a variety of sizes. But the goal is generally the same. The energy transfer is most efficient and stable electric power as much as possible. One of the methods used to achieve this goal is to track the maximum power point. The purpose of tracking the maximum power is**

to ensure that the photovoltaic array energy production or close to the knee point of the curve of the power at all times. The problems of tracking the maximum power point tracking system, that can't power up, when the sun and temperature changes rapidly. The event included a panel partially obscured, so trying to find technical ways to solve such problems. Modern research has focused on the use of neural networks, fuzzy logic and hybrid; to reduce oscillate and entry to the fastest set point values, and also can solve the problem of traditional methods.

Keywords*— *maximum power point, knew point, neural, fuzzy logic, hybrid.

I. INTRODUCTION

Now a day, renewable energy technology has been rapidly developing. Solar energy is a renewable energy that has been developed rapidly and plays a key role in the application of clean energy. But photovoltaic (PV) need to have a maximum power point tracking system that is capable of tracking maximum power. Irradiation and temperature are changing rapidly. Also, when the array is partially shielded. To optimize the output power, there are several ways such as interrupt and observe (P & O), increment conductance (IC), open circuit and short circuit, particle swarm optimization (PSO), fuzzy logic (FL) and hybrid method (HYBRID). This article presents a comparison of the different techniques of modern research that incorporate modern techniques such as Artificial neural network Logic and integration for the fastest response. The presentation of this article enables the selection of maximum power point tracking techniques to be applied. In particular, the comparison of maximum power points between different methods including operating costs, analog or digital, rely on the sensor or not, speed of entry into target value and performance**.**

II. MAXIMUM POWER POINT TRACKING METHOD

A. General Method of Maximum Power Point Tracking

The principle of maximum power point tracking is to extract the maximum solar energy as shown in Fig. 1.

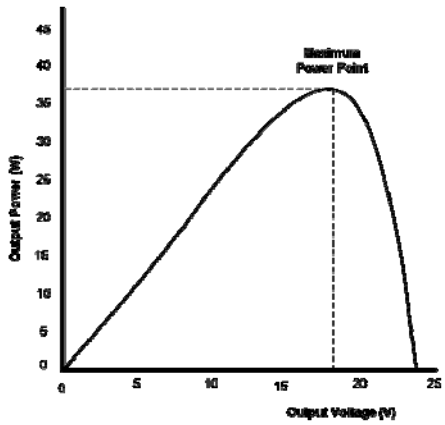

Fig. 1 *Maximum power point.*

There are several ways to get the maximum power of solar energy, such as solar tracking. There are two ways to set up a photovoltaic device, it will cover the system can track the sun, and the other way is to calculate the sun's position. The disadvantage, if the application of the system to control the position error, it is a mistake as well, as shown in Fig. 2.

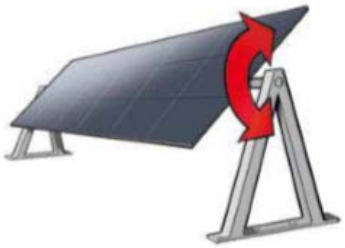

Fig. 2 *Sun's position tracking system [1].*

This system controls solar panels perpendicular to the sun, but loses some of its power to the panel drive system.

The most popular methods is the maximum power point tracking. The advantage of this method is having no moving parts, resulting in lower cost and less energy loss, as shown in Fig. 3.

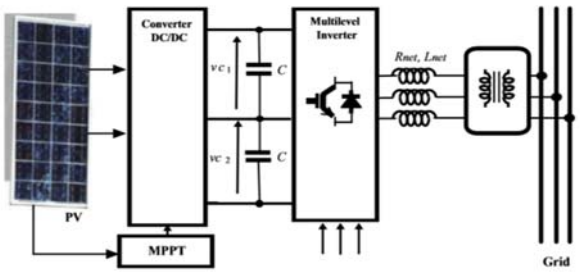

Fig. 3 *Maximum power point tracking method [2].*

Another way is the solar tracking system with maximum power point tracking, which results in the highest possible energy but also the highest cost. Other ways to make the system pay maximum power, such as cooling, but also the cost and energy required to reduce the temperature.

B. Maximum Power Point (MPP)

A several ways of maximum power point tracking (MPPT) such as :

1) A Fixed Percentage of the Open-circuit Voltage

This method is based on the principle that the voltage at the highest power point is linearly correlated with the open circuit voltage. By setting the maximum supply voltage to approximately 76% of the open circuit voltage of the PV array. However, the voltage during open circuit is not constant at any time, so the operation of this method will work as a period by cutting off the load while measure the open circuit voltage, to find the voltage at the peak. The disadvantage of this method, that the load is not continuous. power point is linearly correlated with the open circuit voltage. By setting the maximum supply voltage to approximately 76% of the open circuit voltage of the PV array. However, the voltage during open circuit is not constant at any time, so the operation of this method will work as a period by cutting off the load while measure the open circuit voltage, to find the voltage at the peak. The disadvantage of this method, that the load is not continuous.

2) Perturbation and Observation method : (P&O)

This method will work as a period by comparing the photovoltaic array at the current time with the preceding period. If the rate of change is positive, then the system will adjust the voltage in the same direction, but if the rate of change of power is negative, so the system adjusts the voltage in the opposite direction. The advantage is simple and easy to operate at stable conditions where the amount of light intensity and temperature change slowly. The disadvantage is that if the weather changes rapidly, the system will malfunction.

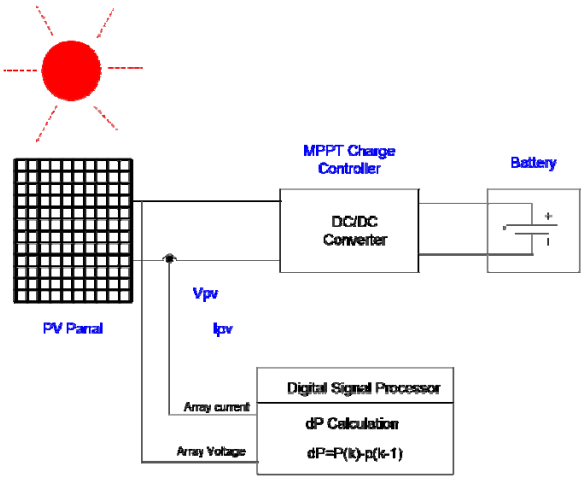

Fig. 4 *Perturbation and Observation method.*

3) Incremental Conductance method : (Inc Cond)

This method is achieved by detecting the voltage and current output of the photovoltaic array, then calculate the rate of change of the power versus the voltage from the equation.

The equation dP/dV=I/V+dI/dV is the increment conductance of photovoltaic array and equation I/V is the rate of change of conductivity. The positive value indicates that the system is running to the left of the maximum power point, then the system will adjust the voltage increase. But, if the result is negative, so the point is at the right of the maximum power point, the system will adjust the voltage drop. However, if the sum is zero, then the system operates at the maximum power point. The system will still have to switch to the original voltage. The advantage is that highly accurate with rapid weather and temperature changes. The disadvantage is quite complicated due to the increased calculation shown in Fig. 5.

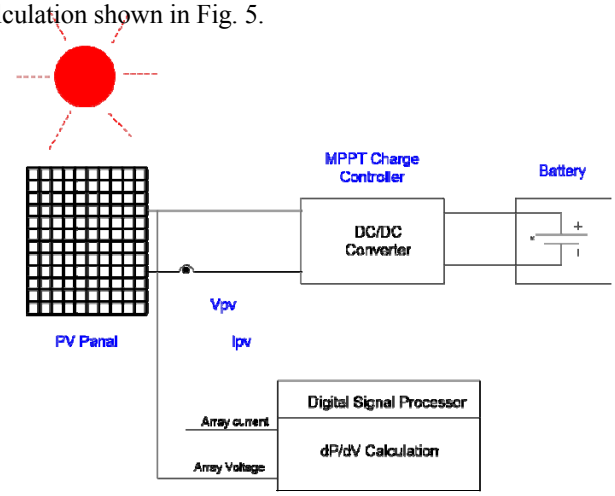

Fig. 5 *Incremental Conductance method.*

TABLE 1 RESEARCH RELATED TO MAXIMUM POWER POINT.

Ref.	Method	Objective	Controller	Result
[1]	NRP-MPPT base on variable step-size INC	Increased precision in control	Matlab/simulink	Fast and accurate MPPT
[2]	FLC-MPPT	Compare between FLC,P&O and INC	Matlab/simulink	The FLC is able to tracking MPP quickly and accurately.
[3]	INC-MPPT base on DC-DC ZETA converter	Transfer power to maximum load	Matlab/simulink	The system is able to tracking MPP quickly when light and temperature change.
[4]	INC and P&O	Comparison between INC and P & O.	Matlab/simulink	P & O performance is better than INC when the system is not linear.
[5]	P&O base on binary-searching with SEPIC converter	Compare BS-P & O with modified P & O and INC.	Matlab/simulinkและ TM4C123G microcontroller	BS-P & O has the best performance and accuracy.
[6]	P&O and INC with soft-switching dc-dc converter/grid connected system	To study the most appropriate method for the system.	Matlab/simulink	INC is the most suitable
[7]	Modified Extremum Seeking MPPT with MVSI	Compare modified Extremum Seeking MPPT with original Extremum Seeking MPPT	Matlab/simulink	Modified Extremum Seeking MPPT is the Faster and more efficient.
[8]	PI- MPPT of SRM load with BAT algorithm	Strengthens the system by comparison with the PSO method.	Matlab/simulink	BAT is superior to PSO
[9]	ANN-MPPT of PMSM load without boost converter and batteries	MPPT when light and temperature change rapidly.	Matlab/simulink	The system is able to tracking MPP quickly as light and temperature change dramatically.
[10]	Modified P&O-MPPT	Develop P & O-MPPT for use with DC micro grids to suit home.	PSIM	The system is able to tracking MPP when light and temperature change rapidly.
[11]	ANFIS-Based PI Controller MPPT	Improve system performance by comparing to INC.	Matlab/Simulink/dPACE	ANFIS tracking MPP faster than INC
[12]	RBFN-MPPT	Fastest MPPT monitoring compared to P & O and INC.	dSPACE1104	RBFN-MPPT is the fastest
[13]	CMOS integrated P & O MPPT	High MPPT Efficiency	CMOS integrated MPPT	System can tracking MPP with High efficiency over 90%
[14]	CV-MPPT and INC MPPT	MPPT of Motor Pump	Matlab/Simulink/dPACE DS1104	CV-MPPT and INC MPPT can tracking MPP
[15]	P & O MPPT with buck-boost converter	MPPT with easy algorithm for PMDC motor	Matlab/Simulink	System can tracking MPP

Another research to optimize the maximum power point is to change from fix step size to variable step size, shown as in Fig. 6.

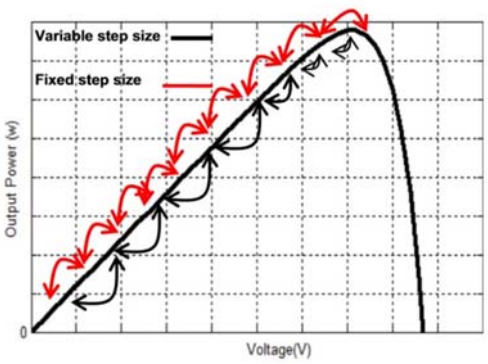

Fig. 6 *Fixed and variable step size MPPT operation.*

The maximum power point tracking method remains the classical method, and has developed new techniques to ensure reliability and efficiency. Fuzzy logic methods (FL) and artificial intelligence method (AI) is a way to find the answer that is used to random the default value and to modify the position of the answer.

The way artificial intelligence is presented in several ways, the structure of the artificial intelligence method is shown in Fig, 7.

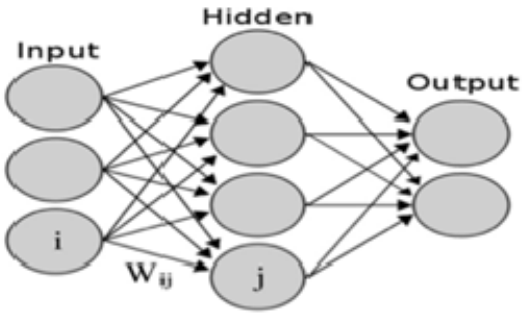

Fig. 7 *Artificial intelligence method [2].*

III. A MODERN RESEARCH EXAMPLE USING THE MAXIMUM POWER POINT TRACKING

1) Real time simulation of MPPT algorithms for PV energy system

Hadjer Bounechba, Aissa Bouzid, Hamza Snani, Abderrazak Lashab

This study presents NRP- MPPT base on variable step-size INC. The objective is increased precision in control, and Matlab/Simulink is used. The result are Fast and accurate MPPT, that is shown in Fig. 8.

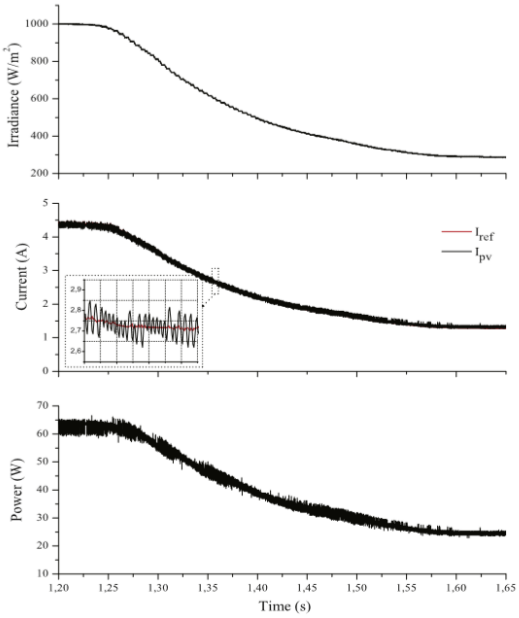

Fig. 8 *Experimental results of the proposed MPPT for variable irradiance [1].*

Fig. 8 is shown the performance of this algorithm a variable irradiance is applied to the PV panel. It can confirm that the proposed algorithm works very well not only if the irradiance is constant but also for a variable irradiance. [1]

2) A three-phase NPC grid-connected inverter for photovoltaic applications using neural network MPPT

Houria Bounaaraf, Abdelaziz Talha, Omar Bouthali

This study presents FLC-MPPT algorithm. The objective is to compare between FLC, P&O and INC. By using Matlab/Simulink, the FLC is able to tracking MPP quickly and accurately, is shown in Fig. 9.

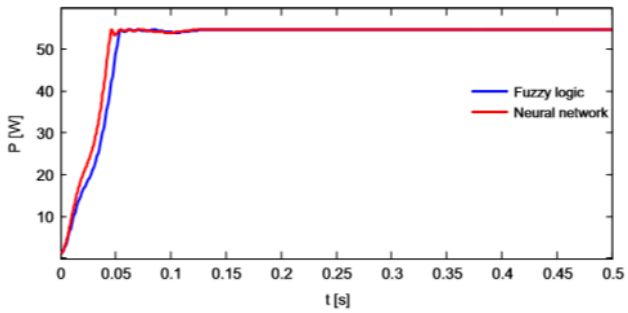

Fig. 9 *System responses in a variable irradiance [2].*

Fig. 9 is shown the performance of neural network algorithm, when a variable irradiance is applied to the PV panel, it can confirm that the algorithm works very well than fuzzy logic algorithm.

IV. CONCLUSION

The modern research related to maximum power point tracking has focused on the artificial intelligence system, fuzzy logic and combination system with artificial intelligence system and fuzzy logic. To solve the problem of traditional systems that can not track the maximum power at rapid changes in temperature and radiation, as well as some shading. By comparison, modern research can solve this problem better than traditional methods, especially artificial intelligence, which makes the system faster to reduce swing. The part requires a highly capable controller with more sophisticated control systems.

ACKNOWLEDGMENT

Express thanks to Rajamangala University of Technology Thanyaburi for their strong support this research.

REFERENCES

[1] Hadjer Bounechba, Aissa Bouzid, Hamza Snani, Abderrazak Lashab, "Real time simulation of MPPT algorithms for PV energy system", Electrical Power and Energy System 83, 2016, pp.67-78.

[2] Houria Bounaaraf, Abdelaziz Talha, Omar Bouthali "A three-phase NPC grid-connected inverter for photovoltaic application using neural network MPPT", Renewable and sustainable Energy Reviews 49, 2015, pp.1171-1179.

[3] A.S Oshaba, E.S.Ali, S.M. Abd Elazim "PI controller design via ABC algorithm for MPPT of PV system supplying DC motor-pump load", Published online:27 May 2016.

[4] Mahdi Rajabi Vincheh,Abbas Kargar, A Hybrid Control Method for Maximum Power Tracking(MPPT) in Photovoltaic System", Arab J Sci Eng, 2014, pp.4715-4725.

[5] Guan-Chyun Hsien, Hung-I Hsieh, ChengYuan Tsai,and Chi-Hao Wang "Photovoltaic Power-Increment-Aided Incremental-Conductance MPPT With Two-Phased Tracking" IEEE Transactions on Power Electronics, Vol.28, No.6 June 2013.

[6] Ahmed A.S. Mohamed, Alberto Berzoy, and Osama A. Mohanmed, "Design and Hardware Implementaion of FL-MPPT Control of PV Systems Based on GA and Small-Signal Analysis", IEEE Transactions on sustainable Energy, Vol 8. No 1, January 2017.

[7] Muamer M. Shebani, Tariq Iqbal, John E.Quaicoe, "Comparing Bisection Numerical Algorithm with Fractional Short Circuit Current and Open Circuit Voltage Methods for MPPT Photovoltaic Systems", IEEE Electrical Power and Energy Conference (EPEC), 2016.

[8] Farhad Khosrojerdi, Shamsodin Taheri, Ana-Maria Cretu "An Adaptive Neuro-Fuzzy Inference System-based MPPT Controller for Pho tovoltaic Arrays", IEEE Electrical Power and Energy Conference (EPEG), 2016.

[9] Marco Balato, Luigi Costanzo, Pompeo Marino, Guido Rubino, Luigi Rubino, Massimo Vitelli, "Modified TEODI MPPT Technique: Theoretical Analysis and Experimental Validation in Uniform and Mismatchig Conditions", IEEE Jouraal of Photovoltaics.

[10] Yaoqiang WANG, Meiling ZHANG, Ming QIN, Xiaoyong MA, "A Practical Step-variation MPPT Scheme for Photovoltaic Power Generation Systems", IEEE, 2016.

[11] Ruben B. Godoy, Douglas B. Bizarro, Elvey T. Andrade, "Procedure to Match the Dynamic Response of MPPT and Droop-Controlled Microinverters", IEEE, 2016.

[12] Manel Hammami, Gabriele Grandi, Massimo Rudam "An Improved MPPT Algorithm Based on Hybrid RCC scheme for Single-Phase PV Systems", IEEE, 2016.

[13] Almas Shintemirov, Bukeikhan Omarali, Farkhat Muratov, Margulan ISSa, "A Sensorless MPPT-based Solar Tracking control approach for mobile autonomous system", IEEE, 2016.

[14] Ping Yang, Yuewu Wang, Qunru Zheng, "Anovel Region Partition MPPT Method Based on Variable Step-size INC", IEEE, 2016.

[15] Ammar Ghalib Al-Gizi, and Sarab Jwaid Al-Chlihawi, "Study of FLC Based MPPT in Comparison with P&O and InC for PV Systems", IEEE, 2016.

On-line PD Detection on Power Generators

Phanupong Fuangpian and Thanapong Suwanasri
The Sirindhorn International Thai-German Graduate School of Engineering (TGGS)
King Mongkut's University of Technology North Bangkok
Bangkok, Thailand
e-mail: phanupong003@hotmail.com

Cattareeya Suwanasri
Department of Electrical and Computer Engineering, Faculty of Engineering
King Mongkut's University of Technology North Bangkok
Bangkok, Thailand

***Abstract*— Generator is the important part in power system. To maintain stability of generator, preventive maintenance is a necessary. Partial discharge (PD) is one of solution to diagnose insulation condition in generator. Therefore, this paper presents on-line PD measurement and example on PD identification in generators. Type of PD can be identified by analyzing the pattern based on Phase-resolved PD. The T-F map is used to separate the phenomena for different kinds of PD source waveforms. The PD patterns of three turbine generators are measured and investigated by commercial tool via capacitive couplers. The results show that PD signals and patterns can be detected in all Phases of three generators. It is found that each PD phenomena in the power generators were not severe. However, the investigation on these PD signals must be timely observed.**

Keywords*— *Parchial Discharge; On-line PD Detection; Stress Grading; Slot Discharge; Generator; T-F Mapping

I. INTRODUCTION

Partial discharge (PD) on generators basically consists of internal discharge, surface discharge and corona discharge [1]. Internal discharge occurs in gas gap inside the insulation. The discharge occurs when the total field inside the cavity is equal to inception field. Surface discharge occurs on insulation surfaces, due to defects between two metallic with different electric field stress. External corona discharge occurs at a sharp metallic point. PD monitoring for rotating machines should be early detected. PD activities and trend from PD measuring tools can be displayed in order to prevent machine failure. Condition-based maintenance can to extend the service life of generators and motors. PD can be detected at generator stator.

The stator components are shown in Fig. 1 [2]. It consists of A) covering tape, B) spacer, coil-end bracin, C) groundwall (main) insulation, mica tapes, D) grading/silicon carbide coating, E) slot semi-conductive coating, F) inner semiconductor coating, G) turn insulation, H) slot wedge/Seal, and I) stator core.

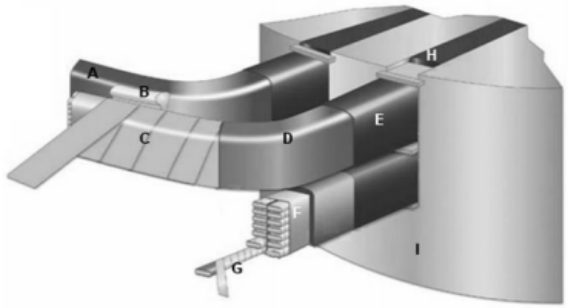

Fig. 1 *Principle of stator winding insulation.*

II. CAUSE OF PD IN STATOR

Damaging of insulation can be caused through combined forces from different stresses such as thermal stress, electrical stress, mechanical stress and ambient stress. Thermal stresses are such as highest and lowest temperature and increase of current through overload. Electrical stresses are operation over rating of rated operating voltage and tested withstand voltage. Ambient stresses such as water, ice can cause rapid degradation. Aggressive and reactive chemicals from gas and acids as well as abrasive particles as metal parts, ash, and carbon also effect the insulation degradation. Finally, oscillation in slot section, mechanical forces in enwinding section, and different thermal expansion are mechanical stresses. The causes of PD in stator windings (from A to L) are presented in Fig. 2. They involve:

A: Small voids on edge

B: Delamination: conductor – main insulation

C: Delamination of tape layers

D: Treeing in layers

E: Broken strands

G: Micro voids

F: Slot discharge, semiconductor paint abrasion

H: Discharges in cooling duct

I: Delamination of insulation in elbow

J: Endwinding surface discharge – contamination

K: Insufficient spacing, tracking and sparking

L: Connection area between slot corona protection and endwinding corona protection.

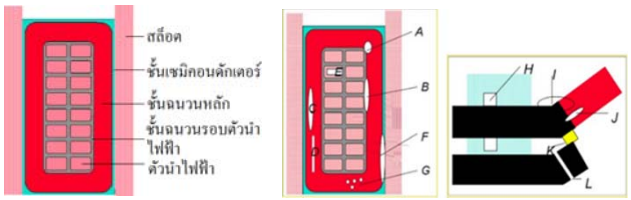

(a) Stator *(b) Insulation failures in generator*

Fig. 2 *Insulation failures in stator windings.*

III. PD Patterns Detected In Generators

The PD pattern on generator can be mainly caused from twelve problems from A to L. Each problem shows the different pattern in Phase Resolved PD (PRPD). Generally, power producers need to be secure on electricity supply to customer. Therefore, the preventive maintenance for power generator is always needed in every 6-8 mounts. In this case, a power producer has found corona noise at generator Unit 1 and suspected other PD in Generator Unit 2 because of the same environment with first generator. Therefore, the investigation on PD was set up to analyze the suspected problem. The results and analyzed are shown in this paper.

A. PD pattern for A: Small voids on edge

As given in Fig. 3, it is internal PD discharge in void. The PD dissipation occurs around 0-90º and 180-270º and it is quite similar wave shapes in both positive and negative cycles. The size of PD depends on size of void.

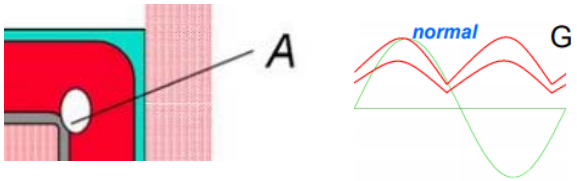

Fig. 3 *Internal discharge in void on edge.*

B. PD pattern for B: Delamination: conductor – main insulation

As given in Fig. 4, it is internal discharges in metal/dielectric-bounded cavity. PD is slightly unbalanced in triangle waveform in positive and negative cycles. PD occurs in advance of system voltage peaks but there are large discharges on one half cycle and small discharge. The amplitude difference on the two half cycles may be as low as 3:1. It is high severity PD.

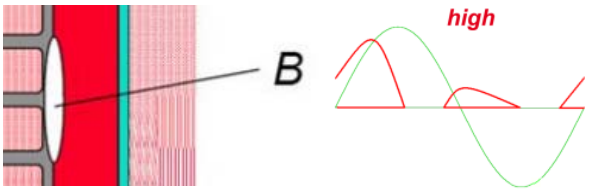

Fig. 4 *Internal discharge in metal/dielectric-bounded cavity.*

C. PD patterns for C: Delamination of tape layers and D: Treeing in layers

As given in Fig. 5, it looks like internal discharge in insulation but the patters are combined with claw patterns in both positive and negative cycles because non-uniform delamination of tape layers and treeings. This causes high severity. In each positive and negative cycle, the PD starts since 0º and 180 º and it keeps increasing till almost 90º and 270º. It is high severity PD.

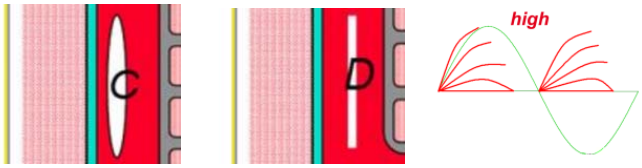

Fig. 5 *Internal discharge with claws in delaminated tape layers and treeing.*

D. PD patterns for E: Broken strands

As given in Fig. 6, it is damage in conductor. The PD pattern should be a combination of internal discharges in metal/dielectric-bounded cavity and arcing. Arcing occurs in gas-insulation media within gap as well as between conductor and solid insulation bounded conductor. It is high severity PD.

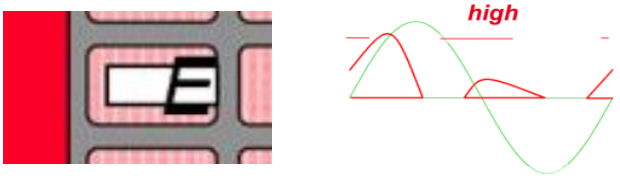

Fig. 6 *Broken strands cause internal discharge in metal/dielectric-bounded cavity and arcing.*

E. PD patterns for F: Slot discharge, semiconductor paint abrasion

As given in Fig. 7, it is internal discharge caused from damage between layers of major insulation, semiconductor and metallic slot. Because there is electric stress in void between metallic slot and major insulation, so the PD shape is closely to case B but is sharply triangle shape. It is high severity PD.

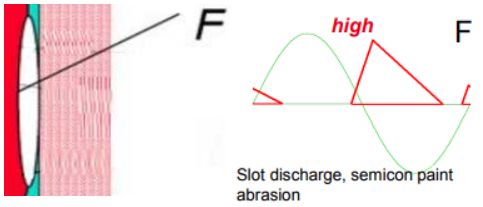

Fig. 7 *Internal discharge between layers of major insulation, semiconductor and metallic slot.*

F. PD patterns for G: Micro voids

Mostly similar to case A, it is internal PD discharge in small voids in insulation. It occurs in advance of system voltage peaks with equal magnitudes on both half positive and negative cycles. It is quite similar wave shapes in both positive and negative cycles. The size and position of PD pattern depends on number, size, shape, and axis of void. It is normal severity PD.

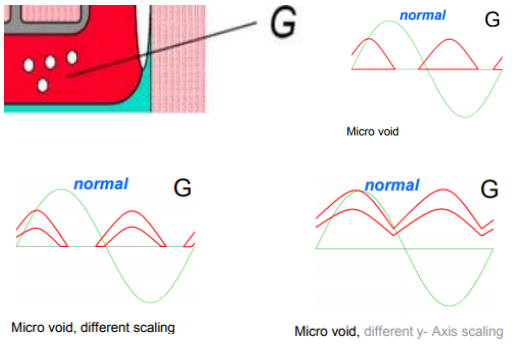

Fig. 8 *Internal discharge between layers of major insulation, semiconductor and metallic slot.*

G. PD patterns for H: Discharges in cooling duct and

I: Delamination of insulation in elbow

As given in Fig. 9, it is surface discharges from metallic conductor to air insulation. It is unbalanced waveform in positive and negative cycles, which occurs in advance of system voltage peaks but there are large discharges on a half positive cycle and small discharges on a half negative cycle. The PD amplitude difference is about 3:1. It is medium severity PD.

Fig. 9 *Surface discharge between bus and air insulation.*

H. PD patterns for J: Endwinding surface discharge – contamination

As given in Fig. 10, Two PD patterns symmetrically dispose on both positive and negative cycles of the supply voltage in rabbit-ear shape. It starts either before or simultaneous supply voltage. On both cycles, patterns are equal in magnitude and opposite in direction. It is low severity PD.

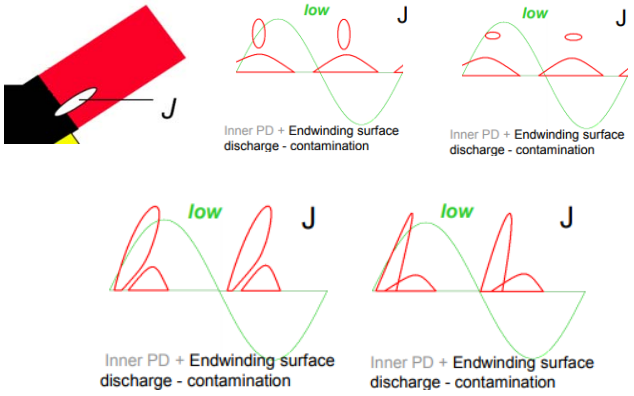

Fig. 10 *Endwinding surface discharge from contamination.*

I. PD patterns for K: Insufficient spacing, tracking and sparking

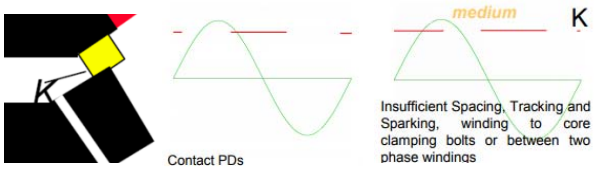

Fig. 11 *Contact produced PD sparking and arcing.*

J. PD patterns for L: Connection area between slot corona protection and endwinding corona protection.

As given in Fig. 12, it is surface discharges from endwinding to air insulation. It is unbalanced waveform in positive and negative cycles, which occurs in advance of system voltage but there are large discharges on a half negative cycle and small discharges on a half positive cycle.

Two PD amplitudes are obviously different in both positive and negative cycles. It is low severity PD.

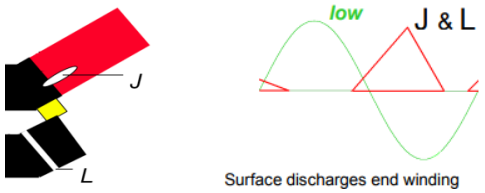

Fig. 12 *Surface discharge between metallic endwinding to air insulation.*

K. PD patterns of noise

Normally, noise pattern is not referring to power frequency and noise amplitude depends on site environment. For generator, noise can cause from power electronic device.

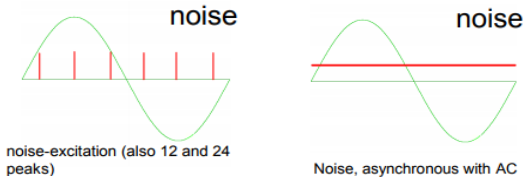

Fig. 13 *Noise patterns.*

IV. PD Detection In Laboratory

PD detection can be divided into two types that are on-line measurement and off-line measurement. The on-line measurement techniques are such as High Frequency Current Transformer (HFCT), acoustic detection and Ultra High Frequency (UHF) detection while the off-line testing techniques are such as high potential (hipot) testing, IEC60270 conventional PD detector [3], power factor and dissipation factor testing, Very Low Frequency testing (VLF). Those PD detection types are used to detect the abnormal condition of the insulation system in high voltage equipments. Moreover, these tools can identify the problem's causes and severity. Then the maintenance can be properly acted.

A. PD Sensors

To measure PD signals at stator model in laboratory, a HFCT sensor is used while to measure the signal at practical generator in power plant high-voltage capacitor couplings is installed.

Current sensor: The high frequency current transformer (HFCT) sensor is shown in Fig.4. The sensor is applied to clamp around the conductor or ground lead of the power cable for PD measurement. PD can cause current pulse with high frequency which flowing to the ground system. The installation of HFCT is shown in Fig.14.

Fig. 14 *HFCT Sensors and installation.*

B. PD Test Circuit in Laboratory

PD detection techniques according to IEC 60270 standard [3], known as conventional method, is widely accepted with the highest accuracy. This technique can describe the phenomena of internal discharge, surface discharge, and air corona. The test circuit is represented in Fig. 15. The circuit comprises supply voltage (AC Source), measuring instruments coupling capacitor (Ck), noise filter (Z), input impedance of measuring system (Zmi), connecting cable, coupling device, measuring instrument and test object (Ca). Then, the discharge patterns can be observed. Some examples on discharge patterns in [1]-[2] are given in Fig. 15.

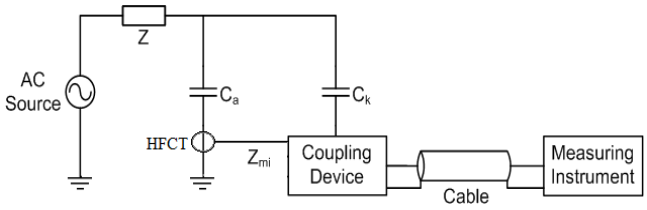

Fig. 15 *IEC 60270 standard for conventional PD test.*

C. I Case Study and Resutls

1) Case study 1: Defect in slot

For Model 1, the air gap was created as shown in Fig.16. The PD measurement result is shown in Fig.17

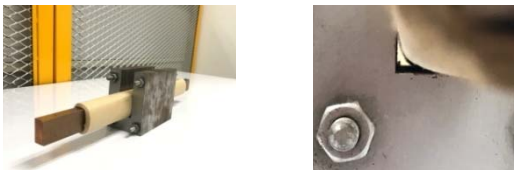

Fig.16 *Air gap model.*

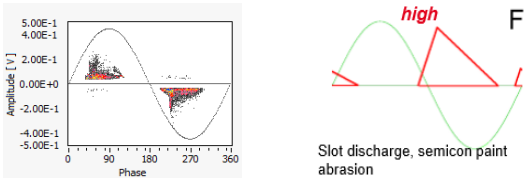

Fig. 17 *Slot discharge pattern from Model 1.*

2) Case study 2: Defect at endwinding

For Model 2, the air gap was created in insulated paper layer as shown in Fig. 18. The PD measurement result is shown in Fig. 19.

Fig. 18 *Model 2: Defect on insulation of endwinding.*

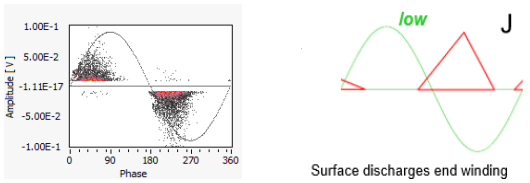

Fig. 19 *Surface discharge pattern from Model 2.*

From the result, the PD pattern measured from Model 2 shows the characteristic as same as the PD pattern from database in type of surface discharge.

3) Case study 3: the air gap on outer layer of insulated paper

For Model 3, the air gap was created on outer layer of insulated paper as shown in Fig. 20. The PD measurement result is shown in Fig. 21.

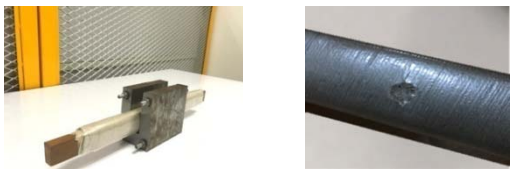

Fig. 20 *Air gap on outer layer.*

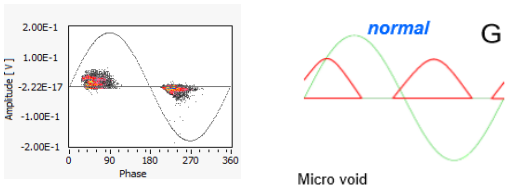

Fig. 21 *Internal discharge pattern from void.*

From the result, the PD pattern measured from Model 3 shows the characteristic as same as the PD pattern from database in type of internal discharge.

V. On-Line For Patial Discharge Detection

In this paper, on-line PD detection on power generator was observed by using unconventional diagnostic commercial tool. The testing equipment includes capacitive coupler, PD detector portable tool and connecting device.

A. Capacitive Coupler

High Voltage Coupling Capacitor (HVCC): The coupling capacitor is shown in Fig.5. The design of capacitive coupler is suitable for permanent installation to measure PD in stator's winding. The PD will cause small voltage drop at origin point which capacitive coupler will transfer electric charge to compensate the dropped voltage at defect point. The installation of capacitive coupler is shown in Fig. 22.

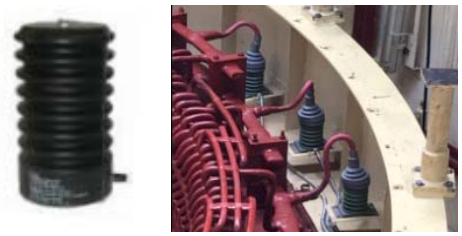

Fig. 22 *Coupling capacitor and installation.*

Capacitive couplers as shown in Fig. 23 are used as the sensors to detect PD signal stator winding. They are connected with main bus bar of the generator at all three Phases. The signal cables (RG58) are used to connect between capacitive coupler and Link Box outside the generator for user interface.

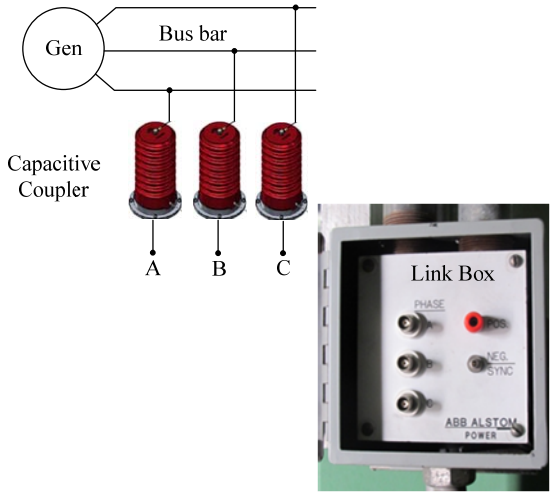

Fig. 23 *Capacitive coupler connected to generator bus bar.*

B. Background Noise

Before any analysis, the background noise must be mitigated. They are caused by the variation in voltage from external source as well as communication signals, resulting to also cause some currents to flow between the source and the capacitance of the system being tested, even without a PD event in the test object. The background noise is detected in commercial tool.

C. Example on On-line Measuring System

Generators Unit 1 and Unit 2 are connected to Link Box via capacitive couplers with 80 pF as presented in Fig. 24 and Fig. 5.Terminal A, B, C are connected to PD detector portable tool, High Pass (HP) filter are needed for noise rejection and PD detector must be synchronized with system voltage of the generator in order to identify the PD using Phase Resolved PD

(PRPD) method. The connecting cables between Link Box and PD detector portable are RG58. Moreover, the WIFI is used to connect between PD detector and computer for acquisition data. The PD software as Graphic User Interface (GUI) is used to analyze the PD pattern as well as PD waveform.

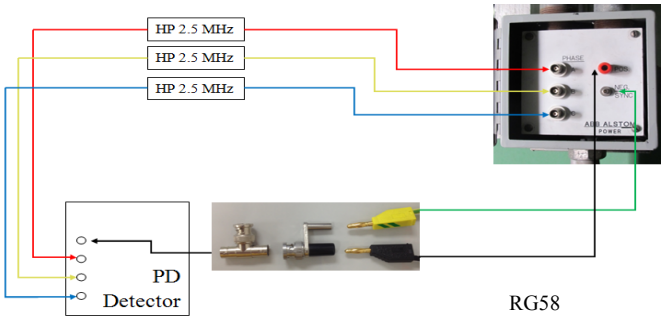

Fig. 24 *Measuring system for generator Unit 1.*

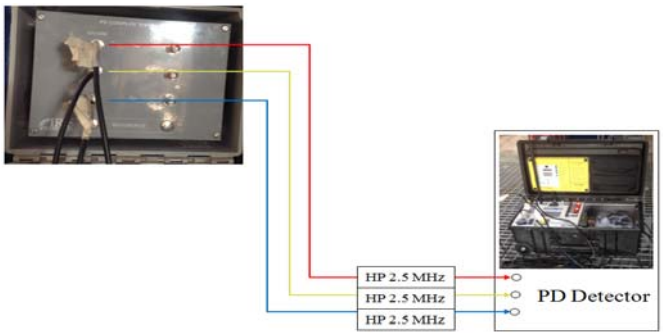

Fig. 25 *Measuring system for generator Unit 2.*

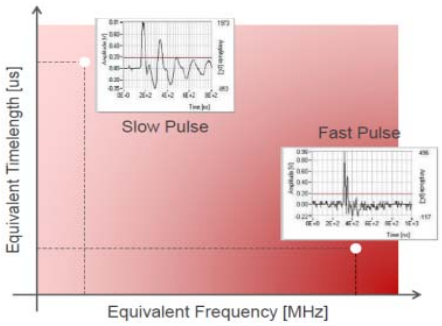

Fig. 26 *Waveforms separated by FFT.*

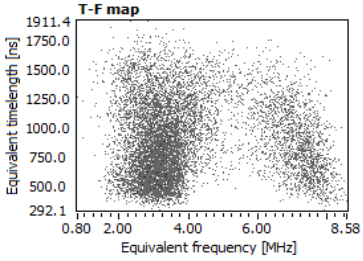

Fig. 27 *Signal phenomena in different parts on T-F map.*

The specification of the PD detector portable commercial tool called the Ultra Wide Brand (UWB) digitizer is 3x100 MS/s, the bandwidth is in between 16 kHz to 35 MHz. Waveform Fast Fourier Transform (FFT) spectrum shows in real time PRPD pattern. The T-F mapping as technology is used to separate the PD phenomena. The process entire waveform of PD pulse is recorded by this tool.

D. T-F Mapping

Fast Fourier Transform (FFT) is applied to separate the signals into different frequencies and time-lengths. Later on, those signals can be plotted into T-F map [5] in order to classify types of signal such as noises or PD pulses. For example, two pluses as slow and fast pluses shown in Fig. 26,they are analyzed and plotted in T-F map as shown in Fig. 27.Finally, these phenomena located in different parts on T-F map are identified the types of signals.

VI. Practical On-Line PD Detection

In this paper, three generators with rated voltage 13.8 kV were measured and investigated by using PD detector. The capacitive couplers with 80 pF were installed at the bus bar in both generators. PDs signal in three Phases of 2 generators were observed and investigated by using PRPD and pulse wave form. The identification was based on pattern in PRPD as worldwide technique [4].

A. Background Noise

Before any analysis, the background noise must be mitigated. They are caused by the variation in voltage from external source as well as communication signals, resulting to also cause some currents to flow between the source and the capacitance of the system being tested, even without a PD event in the test object. The background noise is detected in commercial tool. In this test, background noise lower than 5 mV was removed as shown in Fig. 28.

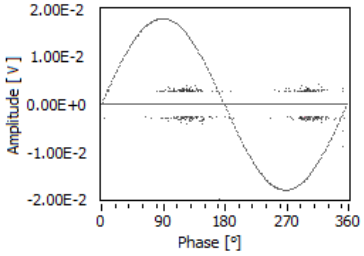

Fig. 28 *Background noise in the system.*

B. PD Detection on Generator Unit 1

For generator Unit 1, the internal PD appeared in all phases with different phenomena. For Phase A, the entire PD pattern in PRPD is separated into two phenomena as given in Fig. 29(a) and 29(b). The causes of two phenomena is analyzed and identified to be distributed microvoids. In Phase B, the entire PD pattern in PRPD can be separated into two phenomena as given in Fig. 30(a) and 30(b). The 1st phenomenon shows stress grading at overhang of Phase B while the 2nd phenomenon is cross-talk from Phase C. In Phase C, the entire PD pattern in PRPD of Phase C is shown

in Fig. 31(a). Similarly, the pattern can be separated into three phenomena as given in Fig. 31(b), 31(c) and 31(d). The first phenomenon shows stress grading at overhang of Phase C while the 2nd and 3rd phenomena are the cross-talk from Phase B.

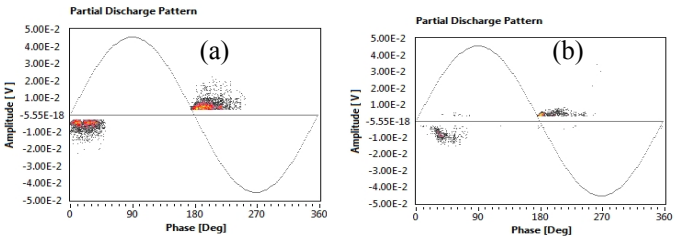

Fig. 29 *PD signal on Phase A of in generator Unit 1 (a) 1st internal PD (b) 2nd internal PD.*

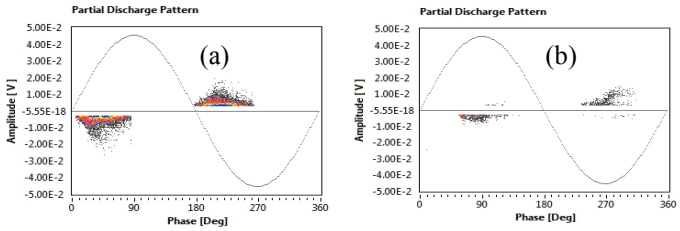

Fig. 30 *Detected signal on Phase B of in Generator Unit 1 (a) 1st phenomenon shows stress grading (b) 2nd phenomenon is cross-talk from another phase.*

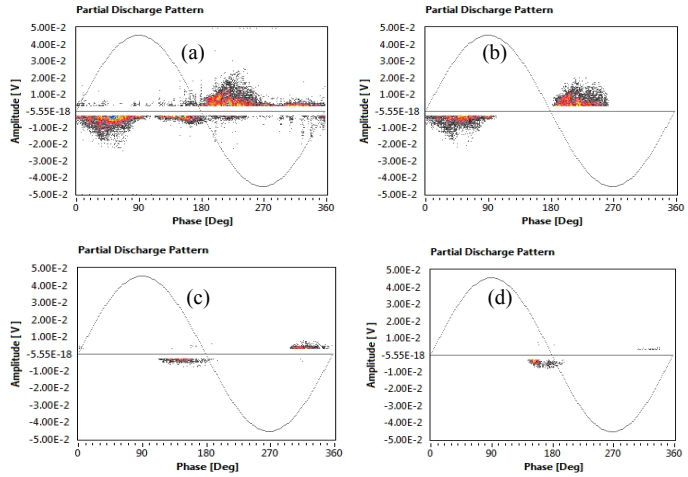

Fig. 31 *(a) Detected PD signal on Phase C of in generator Unit 1 (b) 1st phenomenon shows stress grading (c) 2nd phenomenon is cross-talk from other phase, (d) 3rd phenomenon is cross-talk from other phase.*

C. PD Detection on Generator Unit 2

For generator Unit 2, the PD appeared in only Phase A and Phase C. All patterns are shown in PRPD. In Phase A, two phenomena of distributed micro voids were detected as shown in Fig. 32(a) and 32(b). For Phase B, only cross-talks form Phase A were appeared as shown in Fig. 33(a) - 33(d). In Phase C, the PD is a corona discharge in air gap between bus bars and pressure finger in the region as shown in Fig. 34. It is low severity PD because of low PD magnitude.

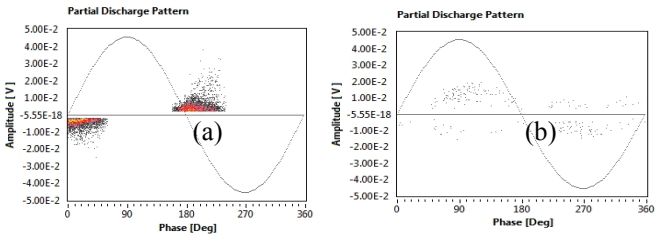

Fig. 32 *PD signal at Phase A in generator Unit 2 (a) 1st internal PD (b) 2nd internal PD.*

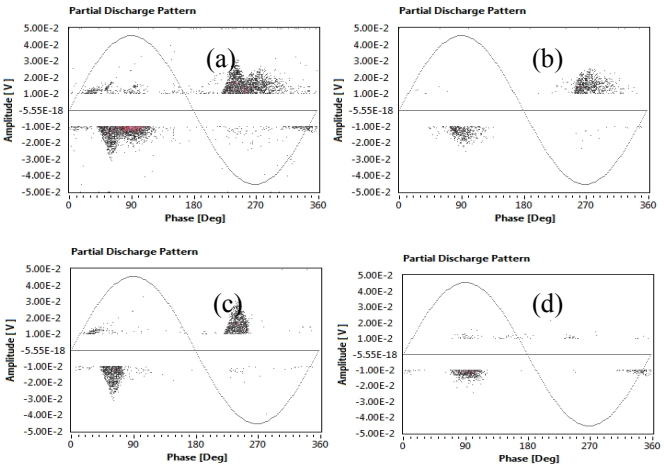

Fig. 33 *PD signal at Phase B in generator Unit 2 (a) Entire detected PD pattern of Phase B (b) 1st cross-talk from Phase A, (c) 2nd cross-talk from Phase A, (d) 3rd cross-talk from Phase A.*

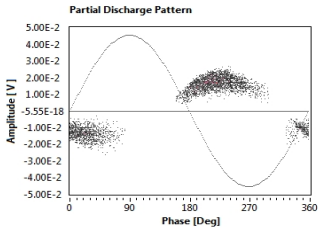

Fig. 34 *Corona discharge in air gap at Phase C in generator Unit 2.*

D. PD Detection on GeneratorUnit 3

For Phase A in Fig. 35(a), the results show that the slot discharge from embedded delamination was detected with amplitude 266 mV. For Phase B in Fig. 35(b), the stress grading discharge at endwinding was found with amplitude 106 mV. For Phase C in Fig. 35(c), the stress grading at endwinding was also detected with amplitude 138 mV. It is medium severity PD. This generator is suggested for a half-yearly investigation.

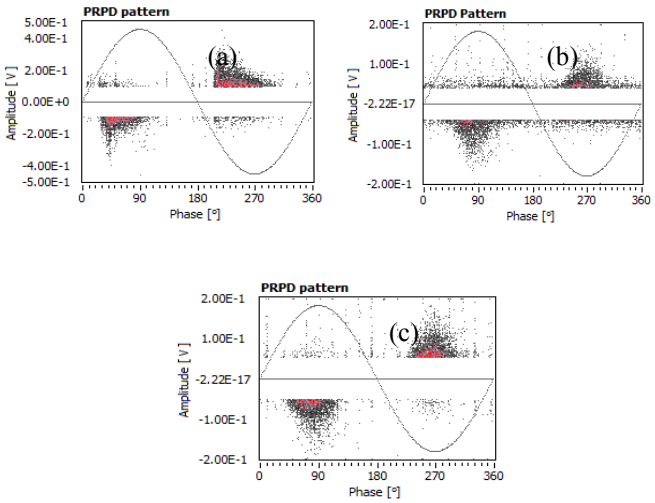

Fig. 35 *PD signal in generator Unit 3 (a) Internal slot discharge at Phase A (b) Stress grading PD of Phase B (c) Stress grading PD at Phase C.*

E. Problem Resolving

In all cases, the amplitudes of PD are not high. Therefore, the PD trend needs to be observed closely. If the PD has higher amplitude and repetition rate, the visual inspection is needed to be taken in effective action. Additional, the on-line PD detection can be used as a on-line monitoring system for observing the insulation damage of power generator and for alarming to any Central Unit (CU) placed in the utility headquarter [6].

VII. Conclusion

The capacitive couplers are used to be sensors for on-line PD detection on power generators. Three power generators as nominal voltage 13.8 kV were investigated. The PDs from different sources and noises in entire PD pattern were separated by using T-F map. In field measurement, the background noise is not stable like in laboratory. Then, the noise should be rejected to clearly show the PD pattern and identify correct problems. The internal PD and stress grading were found in generator Unit 1 with low severity because of low PD amplitude. It is found internal PD from distributed micro voids in generator Unit 2 with also with low severity. For generator Unit 3, both internal slot discharge and stress grading PD were found with medium severity of the amplitude up to 266 mV. In the conclusion, Those PD signals caused from insulation aging can cause the degradation of power generator because of high electric stress, mechanical stress and PD initiation. Therefore, the life extension of generator can be achieved by the good maintenance as condition based-management.

Acknowledgment

The authors thank the independent power producers for on-site PD measurement on generators as well as TGM, Thailand for PD measuring tools from Techimp.

References

[1] CIGRE Working Group 21.03, “Recognition of Discharges,” Electra, No. 11, pp. 61-98, December 1969.

[2] Steffen Moeck, “Monitoring solutions for rotating machines” Training Workshop, OMICRON Energy Solutions GmbH, Berlin, March, 2015.

[3] IEC 60270, “High Voltage Test Techniques-PD Measurements Edition 3”, 2000.

[4] A. Contin, A. Cavallini, G.C. Montanari, G. Pasini, F. Puletti, “Digital detection and fuzzy classification of PD signals”, IEEE Transactions on Dielectrics and Electrical Insulation, Vol. 9, No. 3, pp. 335-348, 2002.

[5] Claude Hudon, Mario B´elec, “Partial Discharge Signal Interpretation for Generator Diagnostics”, IEEE Transactions on Dielectrics and Electrical Insulation, Vol. 12, No. 2; pp. 297- 319, 2005.

[6] L. Fornasari, G.C. Montanari, A. Cavallini, “Alarm Management in permanentPD Monitoring for Generators”, IEEE International Symposium on Electrical Insulation (ISEI), San Juan, Puerto Rico. June 2012.

IEET - International Electrical Engineering Transactions, Vol. 3 No. 2(5) July - December, 2017.

A small PV Source Effect on Ferroresonance Phenomenon in Grid System Integrated using PSCAD

Nattapan Thanomsat
Department of Electrical Engineering,
Faculty of Engineering
Burapha University, Thailand
e-mail: nattapan@eng.buu.ac.th

***Abstract*— This paper presents the effect of ferroresonance in a 400 V line to line or 240 Vrms at low voltage side distribution system integrated with a small PV system in Thailand. This oscillation phenomenon can occur when a small PV system is connected to the LV side of the distribution transformer via three single-phase circuit breaker. The high voltage sides of the distribution transformers are connected to the distribution system via three single-phase circuit breaker. As the saturation property of the transformer cores, ferroresonance can occur when the transformer is switched or disswitched with single-phase switching operation of the circuit breakers. The PSCAD is using to investigate effect the phenomenon of distribution transformer and the current wave form of fast transient can use the equation of current flow in the Dommel's Technique solution. All results will be fully given in this paper. Moreover, the physical phenomena associated to the overvoltage, overcurrent and the damage of distribution transformer are fully discussed.**

Keywords—Ferroresonance, PV Source, Distribution transformer, Dommel's Technique, and PSCAD/EMTDC

I. INTRODUCTION

One of the modern trends in renewable energy is photovoltaic rooftop system integration with distribution grid. Many countries are promoting grid connected PV rooftop system as the components of distributed resources. PV rooftop system can be simply equipped on the frame of rooftop to generate electricity that is used by local loads. For purchaser viewpoint, micro grids can make better the power quality and reliance. There are introduced kind of power quality publish to the power system with the unforecastable nature of the output power and the power electronics components [1]. A lot of research have been done on the modeling system and control of micro grid with hybrid renewable generators [2-6]. However, the power flow of PV system in to the grid can be problematic that overvoltage could be happen in distribution system. The local customer at the daytime used electric is relatively low and distribution network has been utilizing and design to define the effect of voltage drop, not support over voltage. In 2008, the researcher group showed that the distribution network is affected by harmonic from small PV system when connected to the grid [7]. In 2012, another researcher group showed that the low voltage network is affected by voltage rise from PV system when connected to the grid [8].

In additional discussion, the distribution network is affected by operator error or system defects. In low voltage side distribution system, the connecting or disconnecting of line use by manual single phase circuit breaker there are unsymmetrical faults in 3 phase, including no loaded or light loaded distribution transformer and overhead line or underground cable is look like capacitive coupling, that are already high risk for happening ferroresonance. The researcher group reported that the occurrence of ferroresonance are possible to show after some kind of system defect, depend on the system or the type of connections [9]. The transient of overvoltage and overcurrent was produced by this phenomenon and an abnormal power quality in power system. A lot of research groups have studied on ferroresonance in power system and in distribution network [10-17]. A lot of literatures have published on the analysis and simulation of the effects of ferroresonance in power systems [18-23]. All earlier studies, possibility of occurrence ferroresonance have been happen in high voltage side of power system, but possibility of occurrence ferroresonance with the influence of PV rooftop system grid connected on low voltage side distribution transformer in the case has not been considered. This paper studies the effect of PV rooftop system grid connected on low voltage side distribution transformer ferroresonance using Dommel's Technique and simulation using PSCAD.

II. FERRORESONANCE AND ITS EFFECT

The researcher group reported that that ferroresonance is a nonlinear phenomenon which has a chaotic characteristic and may occur in power systems when a nonlinear inductor be able to series with a capacitor and concurrently an unbalance switching or fault happens [13]. Normally, the serious condition that power systems pay attention to ferroresonance are: identity of no or light loaded transformer, single phase switching, and the existence of capacitors. Ferroresonance has some symptoms that thus technician or operator can be aware about its happening. The major problem ones are: over voltage and current, power quality problem, the damaged insulation of apparatus and the defect of protection mechanisms [13].

There are differently ferroresonances in the configuration of power transformer. In 2003, D.A.N. Jacobson reported that examples of ferroresonance in a high voltage power system, there are seven different types of power systems that are

affected to ferroresonance phenomenon [24]. This study chooses one of these seven types of them. The distribution transformer connected and disconnected in one or two phases are modeled and shown in Figure 1. The capacitor is in the form of underground cables or overhead power lines that supply voltage to a transformer primary winding which is connected to a ground.

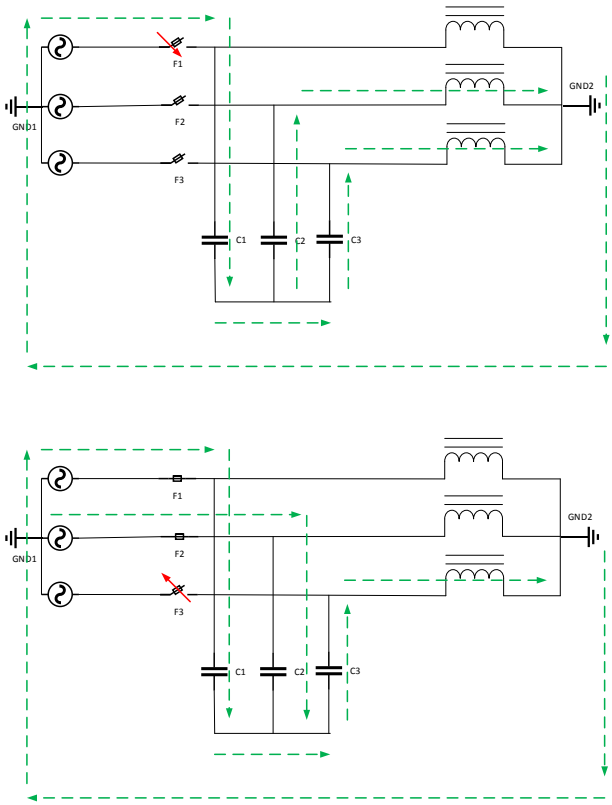

Fig. 1 *Line supplying a transformer with wye-ground connected.*

The connection between the nonlinear inductance and the capacitance may be represented in series or parallel form. In this paper, only series circuit will be considered as shown in Fig. 2.

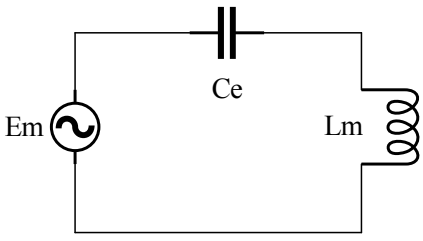

Fig. 2 *Series ferroresonance circuit.*

III. Mathematic Model And Simulation Using By PSCAD

A. Mathematic model in Dommel's Technique

The circuit shown in Figure 2, before reaching the steady state current wave. In this case a closed solution was possible through Laplace and Inverse Laplace transformation technique. In most of the complex, including power system, a closed form of solution is not possible. This is an alternative technique available to solve such complex circuit with reasonable approximation. This method is known as the Dommel's Technique. In this method, all the circuit element such as R, L and C are converted into equivalent resistance and a small time step (t) is used for step-by-step solution. From the figure 2 below, differential equation of circuit flow in the LC circuit.

$$E_m(t) = V_{C_e}(t) + V_{L\,m}(t) \tag{1}$$

$$E_m(t) = C_e \frac{dE_m(t)}{dt} + L_m \frac{di(t)}{dt} \tag{2}$$

And equations of current flow in the Dommel's Technique are

$$E_m(t) = \frac{E(t) + E(t-\Delta t)}{2} \tag{3}$$

$$\frac{dE_m(t)}{dt} = \frac{E(t) - E(t-\Delta t)}{\Delta t} \tag{4}$$

$$\frac{di(t)}{dt} = \frac{i(t) - i(t-\Delta t)}{\Delta t} \tag{5}$$

Substitute eqs. (3), (4) and (5) into (2), then the equation of current flow in the Dommel's Technique solution is given as below.

$$\frac{E(t)+E(t-\Delta t)}{2} = C_e\left[\frac{E(t)-E(t-\Delta t)}{\Delta t}\right] + L_m\left[\frac{i(t)-i(t-\Delta t)}{\Delta t}\right]$$

$$E(t)+E(t-\Delta t) = \frac{2C_e}{\Delta t}\left[E(t)-E(t-\Delta t)\right] + \frac{2L_m}{\Delta t}\left[i(t)-i(t-\Delta t)\right]$$

$$i(t)-i(t-\Delta t) = \frac{\frac{\Delta t}{2}\left[E(t)+E(t-\Delta t)\right] - C_e\left[E(t)-E(t-\Delta t)\right]}{L_m}$$

$$i(t) = \frac{\frac{\Delta t}{2}\left[E(t)+E(t-\Delta t)\right] - C_e\left[E(t)-E(t-\Delta t)\right]}{L_m} - i(t-\Delta t) \tag{6}$$

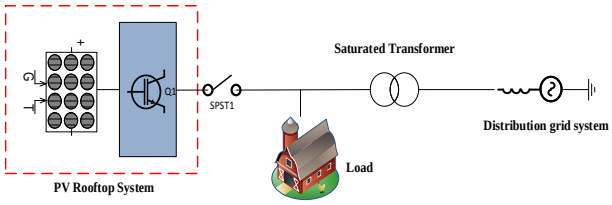

Fig. 3 *the simulation system modeling.*

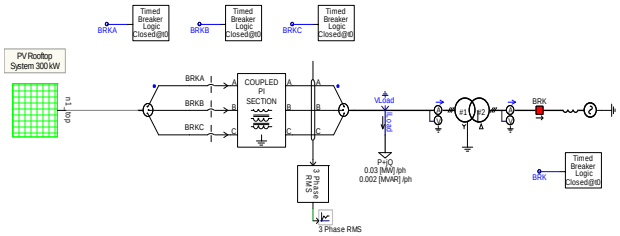

Fig. 4 *the single line diagram simulation system.*

IV. RESULTS

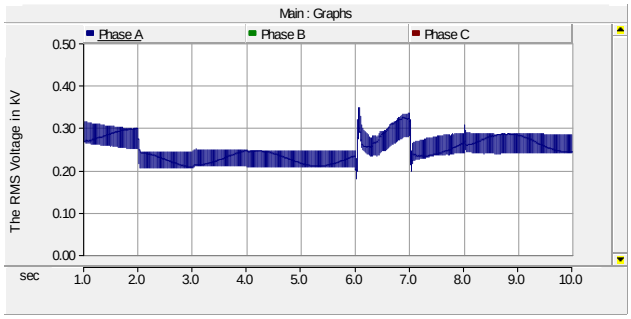

Fig. 5 *The voltage RMS at phase A.*

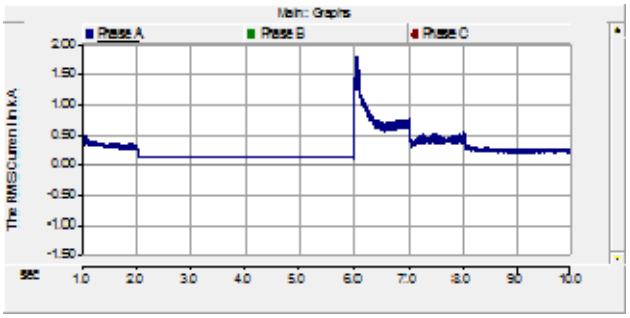

Fig. 6 *The current RMS at phase A.*

The simulation results were followed through for the simulation of various situations affecting ferroresonance and which are indicated in Figs. 5,6, 7, 8, 9, 10, and 11.

First, on phase A, the cutting fuse was breakdown at time 2 sec. and was connected at time 6 sec. The result of RMS voltage and current at phase A is shown in Fig. 5 and 6. After 2 sec., the voltage at phase A was drop from 300 V to 240 V until to 6 sec., the current at phase A drop from 0.25 kA to 0.125 kA. After that, the cutting fuse was connected and the voltage was swing to 350 V at time 6 sec., then at time 8 sec., the voltage was to 300 V. The current was swing to 1.8 kA at time 6 sec., then at time 8 sec., the current was to 0.22 kA.

Second, on phase B, the cutting fuse was breakdown at tim e 3 sec. and was connected at time 8 sec. The result of RMS v oltage and current at phase B is shown in Fig. 7 and 8. After 3 sec., the voltage at phase B was drop from 300 V to 220 V unt il to 8 sec., the current at phase B was oscillated between 0.25 to 0.5 kA in time 2 sec. to 3 sec. and then drop to 0.125 kA. Af ter that, the cutting fuse was connected and at time 8 sec., the voltage was to 290 V. The current was swing to 0.5 kA and dr op to 0.22 kA.

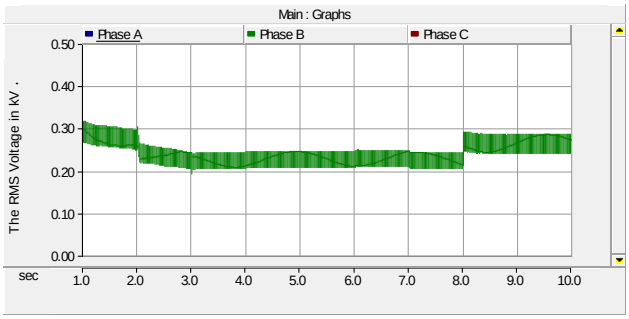

Fig.7 *The voltage RMS at phase B.*

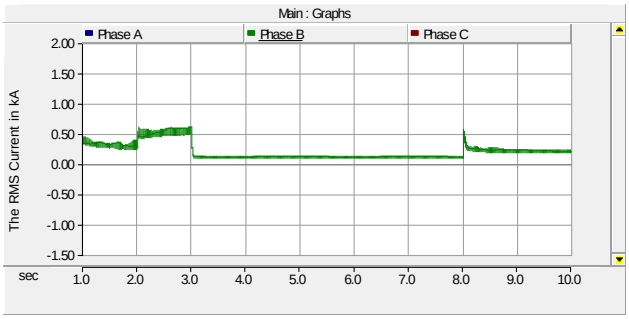

Fig.8 *The current RMS at phase B.*

Finally, on phase C, the cutting fuse was breakdown at time 4 sec. and was connected at time 7 sec. The result of RMS voltage and current at phase C is shown in Fig. 9 and 10. Between 2 to 4 sec., the voltage at phase B was very fluctuation in 220 to 350 V. The current at phase C was oscillated between 0.5 to 1.4 kA in time 2 sec. to 4 sec. and then drop to 0.125 kA. After that, the cutting fuse was connected and at time 7 sec., the voltage was swing to 310 V and drop to 290 V. The current was swing to 0.5 kA and drop to 0.22 kA

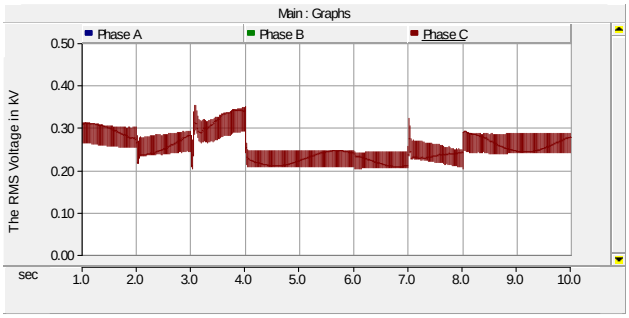

Fig. 9 *The voltage RMS at phase C.*

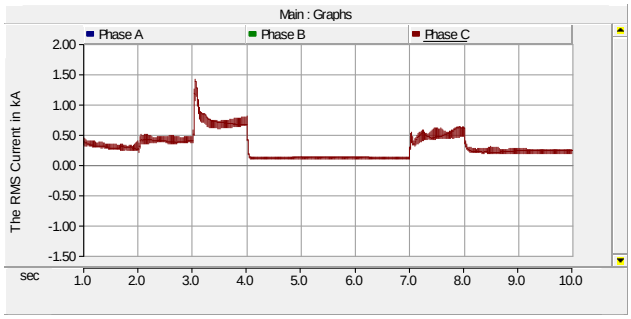

Fig. 10 *The RMS current at phase*

The results point out that the ferroresonance with overvoltage and overcurrent cloud be happen in low voltage side distribution system with under saturation transformer. In addition, the important fundamental of ferroresonace is an unbalanced switching, that the outward manifestation of a sudden change in circuit conditions. Fig. 11 shows the fast transient at phase A after switch is connected. The current waveform can use the equation of current flow in (6) to solve this circuit with reasonable approximation.

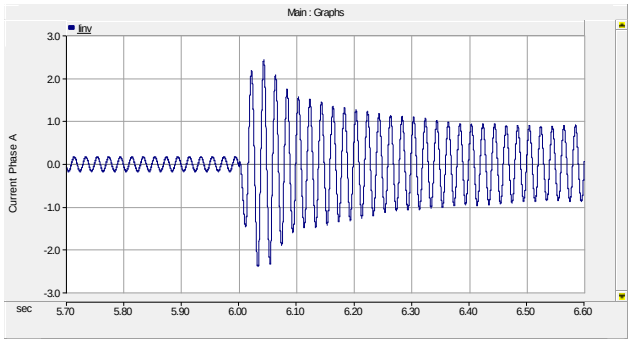

Fig. 11 *Fast transient after switch connected at Phase A*

V. CONCLUSIONS

With this paper, the general effect of the ferroresonance phenomenon was purposed and modeling and simulation studies were realized using PSCAD/EMDTC for the low voltage side 400 V line to line or 240 Vrms at distribution system. The term of the mathematical model were considered, with the Dommel's Technique solution. The results of this simulation were explained and they can be list as follows: In this situation, the ferroresonance causes over voltage and current variations in the low voltage side 400 V line to line or 240 Vrms at distribution system. The over voltage and current variations have fluctuation, that can inject harmonic in to the grid. The over current variation can cause the protection equipment damage. The importance solutions to escape damage of ferroresonance are using a more loss distribution transformer, using three phase circuit breaker and do not connect and disconnect when distribution transformer connected no or light load. In addition, the distribution transformer must be without saturation characteristic.

REFERENCES

[1] Mohammad E. Khodayar, Masoud Barati, Mohammad Shahidehpour, "Integration of High Reliability Distribution System in Microgrid Operation" IEEE Transactions On Smart Grid, Vol. 3, No. 4, December 2012.

[2] O.C. Onar, M. Uzunoglu,, M.S. Alam, "Modeling, control and simulation of an autonomous wind turbine/photovoltaic/fuel cell/ultracapacitor hybrid power system". Journal of Power Sources 185 (2008) 1273–1283

[3] Seul-Ki Kim, Jin-Hong Jeon, Chang-Hee Cho, Jong-Bo Ahn, and SaeHyuk Kwon, "Dynamic Modeling and Control of a Grid-Connected Hybrid Generation System with Versatile Power Transfer" IEEE Transactions on Industrial Electronics, Vol. 55, No. 4, April 2008.

[4] Yu Zhang, NikolaosGatsis, Georgios B. Giannakis, "Robust Energy Management for Microgrids with High-Penetration Renewables". IEEE Transactions on Sustainable Energy, Vol. 4, No. 4, October 2013.

[5] E. Matallanas, M. Castillo-Cagigal, A. Gutiérrez, F. Monasterio-Huelin, E. Caamaño-Martín, D. Masa, J. Jiménez-Leube, "Neural network controller for Active Demand-Side Management with PV energy in the residential sector". Journal of Applied Energy 91 (2012) 90–97

[6] Irvin J. Balaguer, Qin Lei, Shuitao Yang, Uthane Supatti, Fang Zheng Peng, "Control for Grid-Connected and Intentional Islanding Operations of Distributed Power Generation", IEEE Transactions on Industrial Electronics, Vol. 58, No. 1, January 2011

[7] Papaioannou IT, Bouhouras AS, Marinopoulos AG, Alexadis MC, Demoulias CS, Labridis DP., "Harmonic impact of small photovoltaic system connected to LV distribution network." In: Proc. In. conf. IEEE European electricity market, Lisboa, May; 2008. P.1-6

[8] Asnawi Mohd. Busrah, Vigna Kumaran R., "The Impact of grid connected photovoltaic gereration system to voltage rise in low voltage network." In: Proc. In conf. the 3rd International conference on Development, Energy, Environment and Economic (DEEE'12), Paris, France; 2012

[9] C. Stuckens P.A. Monfils N. Janssens Th. Van Craenenbroeck D. Van Dommelen, 'Risk of Ferroresonance in Isolated Neutral Networks and Remedies', CIRED conference,1997, Conference Publication No. 438, O IEE, 1997

[10] KEINY C., "Application of the bifurcation theory in studying and understanding the global behaviour of a ferroresonant electric power circuit" , IEEE Trans.Power Deliv.,1991,6,(2),pp.866-872.

[11] E. J. Dolan, D. A. Gillies, and E. W. Kimbark, "Ferroresonance in a transformer switched with an EVH line," IEEE Transactions on Power Apparatus and Systems, 1972, pp. 1273-1280.

[12] R. P. Aggarwal, M. S. Saxena, B. S. Sharma, S. Kumer, and S. Krishan, "Failure of electromagnetic voltage transformer due to sustained overvoltage on switching*/an in-depth field investigation and analytical study," IEEE Transactions on Power Apparatus and Systems, vol. 5, 1981, pp. 4448-4455.

[13] Z. Emin, B. A. T. A. Zahawi, D. W. Auckland, Y. K. Tong, “Ferroresonance in Electromagnetic Voltage Transformers: A Study Based on Nonlinear Dynamics,” IEE Proc. on Generation, Transmission, Distribution, vol. 144, 1997, pp. 383-387.

[14] J. B. Wareing and F. Perrot, "Ferroresonance overvoltages in distribution networks", in Warning! Ferroresonance Can Damage Your Plant (Digest No: 1997/349), IEE Colloquium on Ferroresonance, Glasgow, Scotland, 1997, pp. 5/1-5/7.

[15] R. A. Walling, "Ferroresonance in low-loss distribution transformers", in Power Engineering Society General Meeting, 2003, IEEE, 2003, p. 1222 Vol. 2.

[16] R. C. Dugan, "Examples of ferroresonance in distribution", in Power Engineering Society General Meeting, 2003, IEEE, p. 1215 Vol. 2., 2003.

[17] H. Radmanesh, A. Abassi, and M. Rostami, “Analysis of Ferroresonance Phenomena in Power Transformers Including Neutral Resistance Effect,” IEEE 2009 conference, Georgia, USA,

[18] C. Stuckens P.A. Monfils N. Janssens Th. Van Craenenbroeck D. Van Dommelen, ‘Risk of Ferroresonance in Isolated Neutral Networks and Remedies’, CIRED conference,1997, Conference Publication No. 438, O IEE, 1997

[19] S.Vinod, Lee. Wei-Jei Jen, ‘The Jump Phenomena’, Industry Applications Magazine’, IEEE, Volume: 14, Issue: 5, 2008

[20] W.Piasecki, M.Florkowski, M.Fulczyk, P. Mahonen, W.Nowak, ‘Mitigating Ferroresonance in Voltage Transformers in Ungrounded MV Networks’, IEEE Transactions on Power Delivery, VOL. 22, NO. 4, OCTOBER 2007

[21] M. Roy, C. K. Roy, ‘Experiments on Ferroresonance at Various Line Conditions and Its Damping’, Power System Technology and IEEE Power India Conference, 2008

[22] M.Fayezizadeh, M.Monadi, F.Shams, S.M.Amini, F.Gheisaripoor, M.Shahpoori, ‘Final Report of the research project about single phase to earth fault in Ramin Power Plant’, Ramin Steam Power Plant, Ahwaz, Iran, 2008

[23] G.Buigues, I.Zamora, V.Valverde, A.J.Mazon, J.I.Sanmartin, ‘Ferroresonance in Three Phase Power Distribution Transformers: Sources, consequences and Prevention’, 19th International Conference on Electricity Distribution, Vienna, May 2007

[24] D. A. N. Jacobson, "Examples of ferroresonance in a high voltage power system", in Power Engineering Society General Meeting, 2003, IEEE, 2003,pp.1206-1212.

IEET Editorial Office

EEAAT - Electrical Engineering Academic Association (Thailand)
Room 409, F-Building
140 Cheum-Sampan Rd.
Nong Chok, Bangkok, Thailand 10530
Tel: +662-988-3655 ext 2216 Fax: +662-988-4026

www.journal.eeaat.or.th